Role of channels in the O_2 permeability of murine red blood cells III. Mathematical modeling

Rossana Occhipinti[1]
Pan Zhao[1]
Fraser J. Moss[1]
Walter F. Boron[1,2]

[1]*Department of Physiology & Biophysics*
Case Western Reserve University School of Medicine
Cleveland, OH 44106
and
[2]*Department of Medicine, and Department of Biochemistry*
Case Western Reserve University School of Medicine
Cleveland, OH 44106

Journal: *Journal of Physiology, Cell physiology*

Running title: *RBC O_2 permeability: Modeling*

Keywords: *Reaction-diffusion model, Hemoglobin, Channel proteins, Unconvected layer, Unstirred layer, Cell membrane*

Correspondence and proofs:

Rossana Occhipinti, PhD
Department of Physiology & Biophysics
Case Western Reserve University
School of Medicine
10900 Euclid Avenue
Cleveland, OH 44106-4970
Phone: (216) 368 3631
Fax: (219) 368 5586
E-mail: rossana.occhipinti@case.edu

Walter F Boron, MD, PhD
Department of Physiology and Biophysics
Case Western Reserve University
School of Medicine
10900 Euclid Avenue
Cleveland, OH 44106-4970
Phone: (216) 368 3400
Fax: (216) 368 5586
E-mail Walter.Boron@case.edu

Key Points

- In this third of three papers, we develop a novel reaction-diffusion model for O_2 offloading from a red blood cell (RBC), treated as a sphere with diameter approximating RBC thickness.
- Using physical constants and parameter values from the literature and papers #1 and #2, we generate simulations that reproduce observed hemoglobin desaturation (rate constant, k_{HbO2}) of intact RBCs from wild-type mice.
- To simulate k_{HbO2} decreases (9%, 17%, 30%) observed in RBCs from knockouts (KOs: aquaporin-1, Rhesus A-glycoprotein, both) we must decrease membrane O_2 permeability (P_{M,O_2}) by far greater percentages (22%, 36%, 55%).
- Analyses of simulated-k_{HbO_2} sensitivity to kinetic and geometric parameters suggest that reasonable parameter-value changes cannot explain experimentally observed k_{HbO2} decreases in RBCs from KOs. Thus, experimentally observed k_{HbO2} decreases must reflect decreases in P_{M,O_2}.
- To accommodate for poikilocytes, we develop a linear-combination approach (poikilocytes + biconcave disks, BCDs) to extract the k_{HbO2} and P_{M,O_2} of just BCDs.

Abstract

In this third of three papers, we develop a reaction-diffusion model for O_2 offloading from a red blood cell (RBC), treated as a sphere with diameter approximating RBC thickness. Stopped-flow (SF) analysis (paper #1) of hemoglobin/oxyhemoglobin (Hb/HbO_2) absorbance spectra during O_2 efflux from intact murine RBCs show that membrane-impermeant inhibitor p-chloromercuribenzenesulfonate (pCMBS) reduces the HbO_2-deoxygenation rate constant (k_{HbO_2}) by ~61%. SF experiments show that k_{HbO_2} falls by (1) 9% for aquaporin-1 knockouts (AQP1-KOs), (2) 17% for Rhesus A-glycoprotein knockouts (RhAG-KOs), (3) 30% for double knockouts (dKOs), and (4) ~78% in dKOs/pCMBS. Here, we simulate HbO_2 dissociation in the intact RBC (i.e., k_{HbO2}); HbO_2, Hb, and O_2 diffusion through RBC cytosol; transmembrane O_2 diffusion; and O_2 diffusion through extracellular unconvected fluid (EUF) to bulk extracellular fluid. Informed by automated-hematology data (paper #1) and imaging–flow-cytometry data (paper #2), simulations predict that observed k_{HbO2} decreases cannot reflect changes only in RBC size/shape or [Hb/HbO_2]. Instead, membrane O_2 permeability (P_{M,O_2}) must fall by (1) 22% to account for AQP1-KO data, (2) 36% for RhAG-KOs, (3) 55% for dKOs, and (4) 91% for dKOs/pCMBS. Exploring predicted k_{HbO2} sensitivities to eight key parameters (e.g., [Hb/HbO_2], diffusion constants, $k_{HbO2\rightarrow Hb+O2}$, thickness_{EUF}, diameter_{Sphere}) shows that no reasonable changes explain the k_{HbO_2} data. We introduce a linear-combination approach to accommodate for the presence of poikilocytes. Finally, contrary to common beliefs, the model predicts that, in the absence of inhibitors, the RBC membrane represents >30% of total diffusive "resistance" to O_2 offloading, even for a WT mouse.

Introduction

Red blood cells (RBCs) are uniquely suited to perform the vital task of taking up oxygen (O_2) in the pulmonary capillaries, carrying this O_2 to the systemic capillaries, and there offloading the O_2 for consumption in the peripheral tissues. This journey of O_2 within the vertebrate body—and the oppositely directed journey of carbon dioxide (CO_2)—involves a series of convective and diffusive steps within and across the various components of the respiratory system.

Integral to the above sequence of events is an important series of membrane-permeation steps, both for O_2 delivery and CO_2 removal. Among the membranes that O_2 and CO_2 must traverse is the plasma membrane of RBCs. The mechanisms by which these gases move across cell membranes, including the RBC membranes, have been the subject of numerous investigations (Graham, 1829, 1833; Mitchell, 1830, 1833; Fick, 1855; Overton, 1895; Wroblewski, 1879; Hartridge & Roughton, 1927; Forster, 1964; Waisbren *et al.*, 1994; Nakhoul *et al.*, 1998; Cooper & Boron, 1998) and reviews (Stannett, 1978; Geers & Gros, 2000; Boron, 2010; Boron *et al.*, 2011; Endeward *et al.*, 2014; Cooper *et al.*, 2015; Michenkova *et al.*, 2021). Prior to the 1990s, two major schools of thought emerged. One, influenced by Krogh's cylinder model of O_2 diffusion from capillary to tissue, implicitly assumes that the RBC membrane offers no resistance to O_2 diffusion (Krogh, 1919; Kreuzer, 1982)—that is, the membrane behaves as a layer of water of equivalent thickness. The other school of thought, influenced by Overton's work on the lipoid nature of plasma membranes, is that the permeability of a membrane to a solute like O_2 depends only on the solubility of the solute in the lipid phase of the membrane (Overton, 1895, 1899).

The present contribution is the third in a series of three interconnected papers[1] that

[1] As a shorthand, we will refer to the three papers as "paper #1", "paper #2", and "paper #3".

investigate the hypothesis that two membrane proteins that are abundant in the murine RBC membrane, aquaporin-1 (AQP1) and the Rh complex (Rh_{Cx})—comprising Rhesus blood group-associated A-glycoprotein (RhAG) and + Rhesus blood group D antigen (RhD)—represent a large fraction of the membrane permeability to O_2 (P_{M,O_2}).

In the first paper (paper #1; Zhao *et al.*, 2025), we employ stopped-flow (SF) analysis of hemoglobin/oxyhemoglobin (Hb/HbO_2) absorbance spectra to measure the rate constant of Hb deoxygenation (k_{HbO_2}) in RBCs from mice genetically deficient in AQP1 (*Aqp1−/−*), RhAG (*Rhag−/−*), or both (*Aqp1−/−Rhag−/−*). In both wild-type (WT) mice and double knockouts (dKO), we also examine the effects of the inhibitors p-chloromercuribenzenesulfonate (pCMBS) and 4,4'-diisothiocyanatostilbene-2,2'-disulfonate (DIDS). Because k_{HbO2} depends on factors other than P_{M,O_2}, we also assess in paper #1 the rate constant of the dissociation $HbO_2 \rightarrow Hb + O_2$ in RBC hemolysates ($k_{HbO2 \rightarrow Hb+O2}$), and automated-hematological parameters, including mean corpuscular volume (MCV), mean corpuscular hemoglobin (MCH), and mean corpuscular hemoglobin concentration (MCHC).

We find that—compared to WT mice—k_{HbO_2} decreases by 9% in RBCs from AQP1-KOs, by 17% in RhAG-KOs, and by 30% in dKO. This work thus points towards roles for AQP1 and RhAG in enhancing O_2 permeation through RBC membranes.

In the second paper (i.e. paper #2; Moss *et al.*, 2025),, we examine RBC morphology at a microscopic scale, and confirm that the RBCs from the KO and dKO mice are predominantly biconcave disks (BCDs). We also use imaging flow cytometry (IFC) to assess RBC major diameter ($Ø_{Major}$). Together with MCV data from paper #1, $Ø_{Major}$ allows us to estimate RBC thickness—a critical piece of information for the simulations in this third (the present) paper in the series. The IFC data also shows that a small fraction of RBCs, more so in drug-treated cells, are poikilocytes, that is, non-biconcave disks (nBCDs). This is also critical information for the present paper because it sets the stage for a novel correction methodology that we apply here. Finally, paper #2

includes a proteomic study that shows that the KO of one or both channels does not affect the apparent abundance of any of the 100 proteins with the greatest inferred abundance.

The purpose of this third (the present) paper in the series is to develop a reaction-diffusion model of O_2 offloading from RBCs, and to use this model—based only on first principles and informed by MCV, MCH, MCHC, $k_{HbO2 \rightarrow Hb+O2}$, and $Ø_{Major}$ data from the first two papers—to simulate the SF data from the paper #1. We find that the simulations agree reasonably well with the time course of deoxygenation for RBCs from WT mice (measured as k_{HbO2} values) in paper #1. Note that our approach is not merely to adjust a variety of fitting parameters in an effort to reproduce the observed k_{HbO2}. Except for sensitivity analyses—when we examine how sensitive the simulations are to variations in specific parameters—the only parameter that we vary is P_{M,O_2}, which we do to predict the P_{M,O_2} values that reproduce the experimentally determined time courses. Our graphical user interface (Huffman *et al.*, 2025) expands the power of the model, especially for non-experts.

Taken together, the three papers argue strongly against each of two previously dominant—and quite opposite—schools of thought (addressed in the Discussion). One holds that RBC membranes offer no resistance whatsoever to O_2 diffusion. The other, posits that they do offer resistance, but that this resistance depends solely on the solubility of O_2 in RBC membrane lipids. Instead, our data are consistent with the notion that RBC membranes from WT mice offer ~150-fold more resistance to O_2 diffusion than an equivalently thick layer of water, and that channels—

AQP1, RhCx, and an unidentified channel(s)—account for >90% of P_{M,O_2} under the conditions of our experiments[2].

2 This manuscript was first published as a preprint: Occhipinti R, Zhao P, Moss FJ & Boron WF (2025). Role of channels in the O_2 permeability of murine red blood cells. III. Mathematical modeling and simulations. bioRxiv. https://www.biorxiv.org/content/10.1101/2025.03.05.639964

Methods

Figure 1 shows the workflow for the three-paper project. The present paper focuses on steps #10, #12 and #12′, #13, #14 and #14′, #16, #17 and #17′, #18 through #22.

Mathematical modeling and simulations

Model formulation. To examine the possibility that changes in RBC parameters—decreases in $k_{HbO2 \rightarrow Hb+O2}$, increases in MCHC (i.e., $[Hb]_i + [HbO_2]_i = [Hb_{Total}]_i$)[3], decreases in diffusion constants (i.e., intra-/extracellular D for O_2; intracellular D for HbO_2, Hb), increases in the thickness of the unconvected-fluid layer that surrounds the cell, or increases in intracellular diffusion distances—can explain our observed decreases in k_{HbO_2}, we developed a distributed (i.e., space-dependent) and dynamic (i.e., time-dependent) reaction-diffusion mathematical model of an RBC—simplified as a perfectly symmetric sphere with diameter equal ($Ø_{Sphere}$) to the thickness of the RBC. Previous modelers have used a sphere in their simulations of an RBC (Vandegriff & Olson, 1984*a*; Williams & Kutchai, 1986; Deonikar & Kavdia, 2013; Deonikar *et al.*, 2014), matching the diameter of the sphere to $Ø_{Major}$. We avoid equating our $Ø_{Sphere}$ with the major diameter of the BCD because this would generate unrealistically large diffusion distances and thus low values of k_{HbO2} and P_{M,O_2}. As described below (see below[4]), our geometrical approach is also unique in that we chose $Ø_{Sphere}$ to match the minor diameter of a torus that has the same volume as

[3] When we use "Hb"—as is standard practice in the literature—without using a subscript designation "T" for tetramer or "M" for monomer, we mean the mass of hemoglobin (in grams), both deoxyhemoglobin (Hb) and oxyhemoglobin (HbO_2). Thus, $[Hb_{Total}]_i$ is the total intracellular Hb concentration—both Hb and HbO_2—measured in g/dl.

[4] See Methods>Mathematical modeling and simulations>Calculation of RBC thickness based on the geometry of a torus. The ">" symbol separates heading levels. It is understood that the reference is to a location in the present paper (i.e., paper #3) unless "See" is followed by "Paper #1" or "Paper #2".

the RBC. In our model (see Figure 2*A*), the spherical RBC is enveloped by a layer of extracellular unconvected fluid (EUF) that is in turn enveloped by the bulk extracellular fluid (bECF). The model accounts for diffusion of O_2, Hb, and HbO_2 within the intracellular fluid (ICF). Only O_2 can move—via diffusion—between the ICF and EUF (i.e., across the plasma membrane, M), within the EUF (which lacks Hb and HbO_2), and between the EUF and bECF (which also lacks Hb and HbO_2). Reactions among O_2, Hb, and HbO_2 occur only in the ICF.

Assuming spherical-radial symmetry, then for each solute *S* (i.e., O_2, Hb, and HbO_2), the concentration (C_S) changes in time (t) and space according to the reaction-diffusion equation

$$\frac{\partial}{\partial t} C_S(t,r) = \underbrace{\frac{1}{r^2}\frac{\partial}{\partial r}\left(D_S(r)\, r^2 \frac{\partial}{\partial r} C_S(t,r) \right)}_{\text{Diffusion term}} + \text{Reaction term}, \quad (1)$$

where r (without a subscript[5]) is the radial distance from the center of the RBC, and D_S is the diffusion coefficient of solute *S*. Figure 2*B* shows the computational domain.

Kinetics of the oxygen-hemoglobin reaction. We model the binding of O_2 to Hb (and dissociation of O_2 from HbO_2)—that is, the reaction term in Equation (1)—as a simple, one-step reaction in which we use a version of the variable-rate-coefficient (VRC) approach proposed by Moll (Moll, 1968). Thus, we assume that each hemoglobin tetramer (Hb_T) is replaced by four independent hemoglobin monomers ($4 \times Hb_M$), and that each hemoglobin monomer can combine with an O_2 via the one-step reaction

$$\mathrm{Hb_M O_2} \underset{k'}{\overset{k}{\rightleftharpoons}} \mathrm{Hb_M} + \mathrm{O_2}\ . \qquad (2)$$

[5] Not to be confused with r_{Torus}, which we use below to describe the minor radius of a torus.

Here, the dissociation rate constant k has the same meaning as $k_{HbO_2 \rightarrow Hb+O_2}$ in paper #1[6], namely, the rate constant for deoxygenation of HbO_2 in an RBC hemolysate; we will use the two notations interchangeably. The rate constant k' for the association reaction is equivalent to $k_{Hb+O_2 \rightarrow HbO_2}$. Rather than assuming that both k and k' are constant—an assumption that would lead to a non-realistic hyperbolic hemoglobin-oxygen saturation curve—we follow a version of Moll's VRC approach, in which we assume that only one of the two reaction rates is constant, while the other one becomes a function of the partial pressure of O_2 (P_{O_2}) so that the mathematical representation of the hemoglobin-oxygen saturation curve corresponds to the measured sigmoidal curve. Yap and Hellums (1987) showed that the VRC model is appropriate in the physiological range, and avoids the use of the more complex Adair model. In his VRC approach, Moll assumed that k' is constant and k is a function of P_{O_2}. However, Clark *et al.* (1985) pointed out that the function used by Moll to describe k as a function of P_{O_2} approaches infinity as P_{O_2} approaches zero. These last authors overcame this problem by assuming that k is constant and k' is a function of P_{O_2}, as described by

$$k' = k \frac{1}{\alpha \times P_{O_2}} \left(\frac{P_{O_2}}{P_{50}} \right)^n , \qquad (3)$$

where α is the solubility coefficient for O_2 in water, P_{50} is P_{O_2} when $[Hb] = [HbO_2]$, and n is the Hill coefficient. With this choice and $n > 1$, k' approaches zero as P_{O_2} approaches zero. Thus, in our model, we follow Clark's variation of the VRC approach, which we implement with the slight modification of substituting $[O_2]$ for P_{O_2}:

$$k' = k \frac{[O_2]^{n-1}}{([O_2]_{50})^n} . \qquad (4)$$

[6] See Paper #1>Methods>Determination of rate constant $k_{HbO_2 \rightarrow Hb+O_2}$ (workflow #11)

Calculation of RBC thickness based on the geometry of a torus. For each mouse strain, we calculate the RBC thickness as follows (Figure 3). We start from the mean major diameter of all RBC-related cell types[7] (e.g., $Ø_{Major}$ = 6.80 μm for WT cells; see paper #2[8])—a measured value—and assume that the RBC is a torus, the outer diameter (OD_{Torus}) of which equals the aforementioned $Ø_{Major}$ (i.e., 6.80 μm in our example). Next, we use the mean corpuscular volume (e.g., MCV = 47.9 pl for WT cells; see paper #2[9])—also a measured value, which we assume to be equal to the volume of the torus (V_{Torus})—to calculate the minor radius (r_{Torus}) of the torus (equivalent to half the thickness of the RBC). Thus, r_{Torus} is a root of the polynomial:

$$2\pi^2 (r_{Torus})^3 - \pi^2 \left(OD_{Torus}\right)(r_{Torus})^2 + V_{Torus} = 0. \qquad (5)$$

The calculated value for the WT cells is r_{Torus} = 1.01 μm. In Table 2, we provide—for each of the 4 mouse strains—the computed values for r_{Torus}, the major radius of the torus (R_{Torus}), and the diameter of the equivalent sphere, where $Ø_{Sphere} = 2r_{Torus}$ (i.e., RBC thickness). The equivalent sphere diameters serve as inputs to our mathematical model.

Calculation of Hb content. For each mouse strain, we calculate the total concentration (both O_2-bound and free, in mM) of Hb tetramers (T)—that is, ($[Hb_{T,Total}]$)[10] —as follows. Based on the hematology data[11] reported in paper #2[9]—specifically, the MCH (in pg) and MCV (in fl)—and

---

[7] These include immature RBCs (i.e., nucleated cells, reticulocytes, and spherocytes) as determined by imaging flow cytometry in paper #2.

[8] See Paper #2>table 3

[9] See Paper #2>table 4

[10] Here we use "Total" to mean all Hb tetramers, whether they bind O_2 (i.e., Hb_TO_2) or not (i.e., Hb_T). Thus, $[Hb_{T,Total}] = [Hb_TO_2] + [Hb_T]$.

[11] These hematology data pertain to the subset of mice used in the imaging flow cytometry and MMM studies.

using a value of 64316 g/mol for the molecular weight of mouse Hb, we calculate the MCHC (in mM). For WT mice, the concentration of total Hb tetramers was ~4.7 mM. However, because our mathematical model deals with monomers, we calculate the concentration of total of Hb monomers ($[Hb_{M,Total}]$)[12] using 4 × MCHC. In the case of RBCs from WT mice, this figure is 18.73 mM. Table 2 lists this value, as well as the comparable values for the other three genotypes. These values inform our mathematical model.

Computational model. In order to solve the system of the three reaction-diffusion equations (1)—one for O_2, one for Hb monomers, and one for HbO_2 monomers—we set the following boundary conditions.

At the center of the RBC, we posit the no-flux Neumann boundary condition:

$$\frac{\partial C_S}{\partial r}(t,0) = 0.$$

At the interface between the ICF and the EUF (i.e., at the M), we establish continuity of Fick's diffusive flux:

$$D_S(R_{Sphere}+)\frac{\partial}{\partial r}C_S(t,R_{Sphere}+) = P_{M,S}\cdot(C_S(t,R_{Sphere}+) - C_S(t,R_{Sphere}-))\ , \tag{6}$$

$$D_S(R_{Sphere}-)\frac{\partial}{\partial r}C_S(t,R_{Sphere}-) = P_{M,S}\cdot(C_S(t,R_{Sphere}+) - C_S(t,R_{Sphere}-)). \tag{7}$$

Here, R_{Sphere} is the radius of the sphere, $C_S(t, R_{Sphere}-)$ is the time-dependent concentration of solute S in the aqueous phase adjacent to the intracellular (−) side of the M; $C_S(t, R_{Sphere}+)$, the comparable

[12] Here we use "Total" to mean all Hb monomers, whether they bind O_2 (i.e., Hb_MO_2) or not (i.e., Hb_m). Thus, $[Hb_{M,Total}] = [Hb_MO_2] + [Hb_M]$.

value on the extracellular (+) side; and $P_{M,S}$ is the true permeability[13] of the membrane to solute *S*. Because O_2 is the only solute that can diffuse across the M, $P_{M,S} \neq 0$ only for $S = O_2$.[14]

In the bECF, we assign Dirichlet boundary conditions and assume that the concentration of O_2 is constant and equal to zero. This assumption is the mathematical equivalent of the annihilation of O_2 by sodium dithionite in our SF reaction cell (see paper #1[15]).

Finally, we set the initial conditions by assuming that, at the beginning of the experiment (i.e., our simulation), no O_2 is present in the EUF, and the free [O_2] everywhere inside the RBC is that dictated by Henry's law for a gas mixture containing 21% O_2. The initial concentrations of O_2, Hb, and HbO_2 in the ICF are those reported in Table 1 for RBCs from WT mice, and in Table 2, for RBCs from mice of each of four genotypes.

We solve the system of the three reaction-diffusion equations (i.e., Eqn (1) for the solutes O_2, Hb, and HbO_2) using the method of lines and the approach described by Somersalo et al for the numerical implementation of the diffusion component (Somersalo *et al.*, 2012). We solve the resulting system of time-dependent ordinary differential equations in Matlab R2015a using the stiff solver ode15s with AbsTol=RelTol=1e–12. The Matlab code is based on the original implementation of Somersalo et al.

---

[13] This is the "permeability" computed on the basis of concentrations immediately adjacent to the two sides of the membrane (i.e., corresponding to $R_{Sphere}-$ and $R_{Sphere}+$). Physiologists usually define permeability operationally, based on the respective concentrations in the bulk intra- and extracellular fluids (see Boron, 2010).

[14] $P_{M,S}$ is the general description for membrane permeability to solute *S*. When *S* is O_2, elsewhere in the three papers, we refer to the permeability as P_{M,O_2}.

[15] See Paper #1>Results>Effect of pCMBS or DIDS on O_2 offloading from RBCs>Stopped-flow Approach

Parameter values. Table 1 lists the parameter values used in the simulation for RBCs from WT mice. Table 2 lists the parameters that we measured in the present study, specific for each of the 4 genotypes; we use these values for computing values for Figure 5. All parameter values correspond to a temperature of 10°C, the temperature at which we perform the stopped-flow experiments (see paper #1[16]). For parameter values not available at the temperature of 10°C, we derive them using Arrhenius equation and values at 25°C and 37°C from references indicated in Table 1. We use this approach for calculating the diffusion coefficient of HbO_2 and HbO_2 in the bulk ICF.

For the diffusion coefficient of O_2 in the bulk ICF, the commonly used value (adjusted for 10°C using the Arrhenius equation, as described above) is 5.09×10^{-6} cm^2 s^{-1} (Clark *et al.*, 1985). More recently, Richardson et al (Richardson *et al.*, 2020) obtained the much lower value of 0.45907×10^{-6} cm^2 s^{-1}. However, we are concerned that this latter value is an underestimate (see Discussion)[17]. We chose to use the arithmetic mean of the commonly used value of 5.09×10^{-6} cm^2 s^{-1} and the more recent value of 0.45907×10^{-6} cm^2 s^{-1}, namely 2.7745×10^{-6} cm^2 s^{-1} (i.e., somewhat more than half the value reported by Clark *et al.*, 1985; see Table 1).

Because the molecular weight of O_2 is much less than the molecular weight of Hb, and because the diffusion coefficient mainly depends on molecular weight, we assume that the diffusion coefficients of monomeric HbO_2 and Hb are the same (Popel, 1989). We assume that the permeability of the RBC plasma membrane to O_2 is 0.15 cm s^{-1}, the value estimated by Endeward et al (Endeward *et al.*, 2006) for the permeability of the RBC plasma membrane to CO_2.

---

[16] See (a) Paper #1>Methods>Physiological Solutions … & … (b) ..>Stopped-flow absorbance spectroscopy (workflow #1)

[17] See Discussion>Recent observations on D_{O_2} in the cytosol of RBC

Simulation of time course of HbO_2 deoxygenation, and estimation of k_{HbO_2}. Using the reaction-diffusion model, we simulate the time course of the decline of HbO_2 saturation (i.e., HbSat = $[HbO_2]/([Hb]+[HbO_2])$ vs. time, employing hematological and morphological data that we gathered for RBCs from WT mice (see Table 1). Because neither the actual nor the simulated time courses of HbO_2 desaturation are precisely exponential, we compute k_{HbO_2} from simulations in a manner analogous to that for our physiological data (see paper #1[18]): we determine the time for the simulated HbSat to fall to $1/e \cong 37\%$ of its initial value (i.e., $\tau_{Quasi} \cong t_{37}$), and then compute k_{HbO_2} as $1/t_{37}$.

Data availability

The data supporting the findings of this study are available within the paper. Any further relevant data are available from the corresponding author upon reasonable request.

[18] See Paper #1>Methods>Calculation of raw-k_{HbO_2} (workflow #3)

Results

The overarching hypothesis of papers #1 and #2 is that AQP1, RhAG, and at least one other RBC membrane protein contribute in a major way to the O_2 permeability of murine RBC membranes.

From a technical perspective, the purpose of this third paper is to develop a reaction-diffusion model—our shorthand for this macroscopic mathematical model is MMM—that is applicable to RBCs in the stopped-flow studies of paper #1. Because our MMM incorporates Fick's first law of diffusion to describe transmembrane O_2 efflux (see Methods)[19] we can relate the input parameter P_{M,O_2}—incorporated into Eqns (6) and (7)—to the output parameter MMM-k_{HbO_2}. As noted in the Introduction, in our simulations, we do not adjust myriad parameter values to match physiological data, but rather use the model to predict—from first principles—the time course of HbO_2 desaturation, which yields MMM-k_{HbO_2}. The input parameters for the simulations are physical constants and values obtained from the literature (see Table 1) as well as values obtained in automated-hematology studies and imaging flow cytometry in papers #1 & #2 (see Table 2). The latter—which include MCV, MCH, and $Ø_{Major}$—allow us to determine values for RBC thickness and total Hb concentration and thereby perform simulations that mimic as closely as possible the conditions of our physiological experiments.

From a philosophical perspective, our purpose in the present paper is to use simulations based on the MMM to make a series of estimates of P_{M,O_2} that generate a series of MMM-k_{HbO_2} values that allow us to hone in on our best estimate of P_{M,O_2} in a particular set of stopped-flow experiments in paper #1.

---

[19] See Methods>Mathematical modeling and simulations>Model formulation

If our hypothesis is correct, RBCs from mice genetically deficient in AQP1, RhAG, or both ought to have lower P_{M,O_2} values when compared to RBCs from WT mice. In order to test our hypothesis, we must assess P_{M,O_2} from experimental data. In paper #1[20], we use SF absorbance spectroscopy to measure k_{HbO_2} of RBCs from mice genetically deficient in AQP1, RhAG, or both. We find that, when compared to WTs, k_{HbO_2} decreases by 9% in AQP1-KOs, 17% in RhAG-KOs, and 30% in dKOs. Moreover, k_{HbO_2} decreases by 53% in dKO RBCs treated with DIDS, and by 78% in dKO RBCs treated with PCMBS. One might immediately ask why the sum 9% + 17% is not precisely 30%? The answer, aside from experimental and rounding errors, is that P_{M,O_2}—the presumed target of our genetic and pharmacological manipulations—is only one element that contributes to MMM-k_{HbO_2} (see Figure 2*A*), resulting (as we shall see later) in a curvilinear dependence of P_{M,O_2} on $\log(k_{HbO_2})$.

In the following sections we show that, by informing the model with reasonable parameter values and internally consistent (i.e., gathered in our laboratory) hematology and flow cytometry data, our MMM model provides reasonable estimates of the time course of HbO_2 desaturation and corresponding MMM-k_{HbO_2}. Moreover, the model confirms that decreases in the value of k_{HbO2} correspond to decreases in P_{M,O_2}, thereby supporting the hypothesis that membrane proteins like AQP1 and the mouse Rh complex (Rh_{Cx} = RhAG + RhD) contribute to P_{M,O_2}.

Simulations of O_2 efflux from a control RBC of WT mouse

Our first goal was to establish an in-silico experiment that would mimic O_2 efflux from a control (Ctrl; i.e., not pretreated with inhibitors) RBC of a WT mouse (WT/Ctrl). For this simulation, our input parameters are those reported in Table 1, which includes physical constants

[20] See Paper #1>Results>Effect of genetic deletions on O_2 offloading from RBCs

and values obtained from the literature as well as values for RBC thickness and total Hb concentration obtained from our hematological and morphological data (i.e., MCV, MCH, $Ø_{Major}$) of WT mice (see Table 2), first column).

Figure 4 shows results of this simulation. At the top of the figure, panels *A*, *B*, and *C* show the time courses of the intracellular (i) concentrations of free O_2, HbO_2, and the sum of free O_2 + HbO_2—integrated over the entire volume of the cytoplasm—as O_2 diffuses out of the cell in a simulated O_2-offloading experiment, as in paper #1[21].

$[O_2]_i$. As expected, because O_2 is leaving the cell, $[O_2]_i$ decreases (Figure 4*A*).

$[HbO_2]_i$ and $[O_2]_i + [HbO_2]_i$. At the same time as $[O_2]_i$ decreases, $[HbO_2]_i$ decreases (Figure 4*B*) in parallel with intracellular $[O_2]_i + [HbO_2]_i$ (Figure 4*C*). These three time courses in Figure 4*A*-*C* reflect (1) the efflux of free O_2; (2) the diffusion of free O_2 toward the membrane; (3) the net reaction $HbO_2 \rightarrow Hb + O_2$, which consumes HbO_2 to produce free Hb and free O_2 and continues until HbO_2 is fully depleted; (4) the diffusion of HbO_2 toward the membrane, and (5) the diffusion of free Hb away from the membrane. The time courses of $[HbO_2]_i$ and of $[O_2]_i + [HbO_2]_i$ are nearly identical because $[O_2]_i << [HbO_2]_i$.

At the bottom of the figure, panels *D*, *E*, and *F* show the time courses of hemoglobin saturation, $[Hb]_i$, and the O_2 efflux across the plasma membrane (J_{M,O_2}).

HbSat. As expected, HbSat falls (Figure 4*D*) with a time course that is similar to that of $[HbO_2]_i$ (see Figure 4*B*). It is from this time course of HbSat that we calculate the MMM-k_{HbO2} of

[21] See Paper #1>figure 3*d*, dark-green curve

WT/Ctrl RBCs (see Methods[22]). The model predicts a MMM-k_{HbO2} of ~3.99 s^{-1}, which will become our "Provisional MMM-k_{HbO2}" in our accommodation for nBCDs (see below[23]).

$[Hb]_i$. As anticipated, $[Hb]_i$ increases (Figure 4*E*) with a time course that is the inverse of that of $[HbO_2]_i$.

J_{M,O_2}. Finally, J_{M,O_2} initially zero, spikes rapidly to a maximal value, decays rapidly to a value somewhat above zero, and finally drifts toward zero (Figure 4*F*). The J_{M,O_2} upward spike reflects the large initial transmembrane O_2 gradient. The rapid decay reflects O_2 depletion near the inner surface of the membrane. The O_2 efflux during the slower decay is supported by O_2 that diffuses to the inner surface of the membrane from the depths of the RBC and, to a much lesser extent, the parallel diffusion and dissociation of HbO_2.

Predicted k_{HbO2} values from simulations of control RBCs from WT and KO mice, as informed by genotype-specific hematological, morphological, and kinetic data

Besides P_{M,O_2}, the MMM-k_{HbO2} that describes O_2-offloading from RBCs depends on several genotype-specific parameters: $Ø_{Sphere}$ (which in turn depends on MCV, $Ø_{Major}$, and RBC shape), $[Hb_{Total}]_i$ (computed from MCHC), and $k_{HbO2 \rightarrow Hb+O2}$ (i.e., the same as k in Eqn (2); determined on SF experiments on RBC hemolysates). To investigate whether the decreases in k_{HbO2} observed in RBCs from KOs (see paper #1[24]) could be explained by changes in parameters

---

[22] See Methods>Mathematical modeling and simulations>Simulation of time course of HbO_2 deoxygenation, and estimation of k_{HbO2}

[23] See Results>Accommodation for non-BCDs

[24] See Paper #1>figure 5*b*

other than P_{M,O_2}, we as a first step gathered the requisite genotype-specific data in paper #1 and paper #2. We provide these parameter values in Table 2. Note the trend (from left to right) for MCV to increase in the KOs, but for MCHC to decrease. In addition, using a battery of methodologies to assess RBCs shape (blood smears, still/video images of living RBCs, and imaging flow cytometry), we find that ~98% of control RBCs, both from WTs and dKOs, are biconcave disks (see paper #2[25]).

To assess the effects of the genotype-specific differences summarized in Table 2, we perform simulations in which we mimic control RBCs (i.e., not pretreated with inhibitors) from WT, AQP1-KO, RhAG-KO and dKO mice. Note that the simulation for a control WT RBC is the same one that yielded the MMM-k_{HbO_2} of 3.99 s^{-1} in the previous section. We simulate O_2 efflux from RBCs of AQP1-KO/Ctrl, RhAG-KO/Ctrl, and dKO/Ctrl mice using the same parameter values (including P_{M,O_2}) that we used for WT/Ctrl RBC (see Table 1) with the exception of the genotype-specific values in Table 2 for $Ø_{Sphere}$ (mimicking RBC thickness) and $[Hb_{M,Total}]_i$ (a surrogate for MCHC).

Figure 5 shows a pair of MMM-k_{HbO_2} values for each of the four genotypes. In these simulations we assume that all RBCs are intact, as they are for the hemolysis-corrected (HC) k_{HbO_2} values in paper #1, and that all cells are BCDs, as they are for the shape-corrected (SC) k_{HbO_2} values for SF experiments in paper #1[26]. In Figure 5*A*, we compute MMM-k_{HbO_2} values using our standard $k_{HbO_2 \rightarrow Hb+O_2}$ value of 11.6 s^{-1} (see Table 1), which is an average for all four genotypes. We use this standard value for all simulations here in paper #3 (including Figure 5*A*) except for

[25] See Paper #2>figure 8*b*–*c*, "Ctrl" bars

[26] See Paper #1>figure 5*b*

those in Figure 5*B*, where we use four separate, genotype-specific $k_{HbO2 \rightarrow Hb+O2}$ values (see Table 2).

The solid green bars in both Figure 5*A* and *B* correspond to an MMM-k_{HbO2} of ~3.99 s^{-1} for a WT/Ctrl RBC (i.e., no drugs). Both panels have the same MMM-k_{HbO2} value because, by serendipity, the standard $k_{HbO2 \rightarrow Hb+O2}$ is virtually the same as the genotype-specific value for WT/Ctrl RBCs.

The pink bar in Figure 5*A* simulates an AQP1-KO/Ctrl RBC; MMM-$k_{HbO2} \cong 4.04$ s^{-1}, which is a predicted 1.1% increase vs. 3.99 s^{-1}, rather than the 9% decrease observed in paper #1. In Figure 5*B*, MMM-k_{HbO2} is ~4.10 s^{-1}, which represents an even larger increase, 2.6%.

The blue bar in Figure 5*A* simulates a RhAG-KO/Ctrl RBC; its MMM-k_{HbO2} of 3.82 s^{-1} represents a predicted decrease of 4.4%, rather than the 17% decrease observed in paper #1. The corresponding MMM-k_{HbO2} in Figure 5*B*, is ~3.85 s^{-1}, which predicts a somewhat smaller decrease of 3.5%.

Finally, the purple bar in Figure 5*A* simulates a dKO/Ctrl RBC; its MMM-k_{HbO2} of 3.85 s^{-1} is a decrease of only 3.7% vs. WT/Ctrl, rather than the ~30% decrease in paper #1. In Figure 5*B*, MMM-k_{HbO2} is ~3.74 s^{-1}, which predicts a decrease of 6.3%, which is still far smaller than what we observed in paper #1.

Thus, we conclude that the genotype-specific changes reported in paper #1 and paper #2—and summarized here in Table 2—cannot explain the observed KO-induced decreases in SC-k_{HbO2} in paper #1. We intuit that the effects of anti-parallel increases in MCV and decreases in MCHC tend to cancel, and thereby tend to minimize the impact on MMM-k_{HbO2} values. We examine this

possibility in the sensitivity analyses, below[27]. We conclude that KO-induced variations in RBC dimensions, $[Hb_{Total}]_i$, and $k_{HbO2 \rightarrow Hb+O2}$ cannot account for the KO-induced decreases in SC-k_{HbO2} observed in paper #1.

Predicted dependence of O_2 offloading (k_{HbO2}) on the O_2 permeability of RBC membrane (P_{M,O_2})

In the previous sections, we show that our MMM—with a fixed P_{M,O_2} and genotype-specific values for other parameters—can mimic the time course of O_2 offloading (i.e., MMM-$k_{HbO2} \cong$ SC-k_{HbO2}) for a control RBC from a WT mouse, but not for control RBCs from any of our three KO groups. Clearly, we must invoke some other parameter to account for the control and KO data in paper #1 and, by extension, the paper-#1 data on inhibitors and KO+inhibitors. We hypothesize that this other parameter is P_{M,O_2}. (In the case of drug-treated RBCs, we will apply a shape correction, described below, to accommodate the appearance of nBCDs, i.e., poikilocytes).

Having established an in-silico approach for WT/Ctrl experiments, we can now employ the model to answer the two key questions that are at the core of our investigation:

1. What is the dependence of MMM-k_{HbO_2} on P_{M,O_2}? This will help us understand the extent to which observed decreases in SC-k_{HbO_2} in paper #1 correspond to decreases in P_{M,O_2}?
2. Can we use physiological k_{HbO_2} measurements to make predictions about P_{M,O_2}?

To answer these questions, we employ the model that mimics a control WT RBC (i.e., input parameter values listed in Table 1) and perform a series of more than 70 simulations in which we

[27] See Results>Mathematical simulations exploring the predicted sensitivity of k_{HbO2} to eight key kinetic and geometric parameters

systematically vary P_{M,O_2} while holding all other parameters constant. Throughout, we assume that the RBCs are biconcave disks so that we need not accommodate for shape changes. Thus, by definition, the MMM-k_{HbO_2} is analogous to the SC-k_{HbO_2}. The continuous curve in Figure 6 is a semi-logarithmic plot showing the dependence of MMM-k_{HbO_2} (y-axis) on P_{M,O_2} (x-axis, scaled logarithmically). The shape of this curve depends on the parameters in Table 1, and thus could vary with each strain of mouse, and each species (see Discussion[28]).

The point at the extreme upper-right—labeled "H_2O membrane"—represents the hypothetical situation in which we assume that the plasma membrane—as is implicit in Krogh's calculations—is a thin film of H_2O of equivalent thickness. That is, for the plasma membrane, we assume that the diffusion constant D_{O_2} has the same value as in free water, namely 1.3313×10^{-5} $cm^2\ s^{-1}$, which translates to a P_{M,O_2} of ~22.63 cm s^{-1}. In our simulations, this value generates a MMM-k_{HbO2} of ~6.00 s^{-1}. For the given geometric, hematologic, and kinetic parameters, this point represents the maximum-possible values for P_{M,O_2} and thus the maximum-possible rate of O_2 offloading.

What is the position of a WT/Ctrl RBC on this curve? Note that (1) WT/Ctrl RBCs have an nBCD prevalence of 1.41% (see paper #2[29]) and (2) nBCDs (because of their larger spherical diameter; see paper #2[29]) are expected to have a lower O_2-offloading rate that BCDs. The MMM-k_{HbO_2} of 3.99 s^{-1}—which we have already generated using P_{M,O_2} = 0.15 cm s^{-1}—in fact pertains not to a pure population of BCDs, but rather to a mixture of 98.59% BCDs and 1.41% nBCDs. Our accommodation for nBCDs presented below[30]) leads to the conclusions that (1) the actual

---

[28] See Discussion>Uniqueness of the sigmoidal k_{HbO_2} vs. log(P_{M,O_2}) curve

[29] See Paper #2>table 5

[30] See Results>Accommodation for non-BCDs

k_{HbO2} for the BCD component is ~4.04 s^{-1} vs. 3.99 s^{-1} for the mixture, and (2) the actual P_{M,O_2} for both BCDs and nBCDs is 0.1546 cm s^{-1}, which is ~3.1% higher than our provisional value of 0.15 cm s^{-1}. Thus, the point labeled "WT/Ctrl" in Figure 6 has the shape-corrected coordinates (P_{M,O_2} = 0.1546 cm s^{-1}, k_{HbO2} = 4.0358 s^{-1}) and is our best estimate of a pure population of BCDs.

Note that the P_{M,O_2} of 0.1546 cm s^{-1} for WT/Ctrl BCDs is only ~0.7% as large (or ~1/150) as the hypothetical P_{M,O_2} of Krogh's pure-water membrane. In other words, the RBC membrane offers 150-fold more resistance to O_2 diffusion than would a film of H_2O.

Besides WT/Ctrl, each of the seven other labeled points in Figure 6 corresponds to one of the other experimental conditions. For each point, we determine the y-axis value (MMM-k_{HbO2}) by performing the shape correction described below[30] (steps #13 – #22 in Figure 1), based on experimentally determined parameter values. We determine the x-axis value (P_{M,O_2}) by interpolation (step #19 in Figure 1), thereby placing the point on the sigmoidal curve. Note that the dKO/Ctrl and the WT/DIDS points nearly overlap.

Table 3 summarizes the key numerical values corresponding to the eight experimental points in Figure 6. Our standard condition is WT/Ctrl (upper-left corner of table), for which the shape-corrected values are SC-P_{M,O_2} = 4.0358 s^{-1} and SC-P_{M,O_2} = 0.1546 cm s^{-1}. Compared to these standard SC values, the AQP1-KO/Ctrl has an SC-P_{M,O_2} that is 21.56% lower, and an SC-k_{HbO2} that is 8.85% lower—and so on for the other conditions. Note that the sum of the computed % decreases in P_{M,O_2} for AQP1-KO/Ctrl (~22%) and RhAG-KO/Ctrl (~36%) is nearly equal to the computed P_{M,O_2} % decrease for the dKO/Ctrl (~55%). The largest % decrease in P_{M,O_2} occurs with dKO/pCMBS (~91%). The effects of the membrane-protein knockouts and inhibitors on P_{M,O_2}—

along with the proteomics data in paper #2[31]—supports the hypothesis that the vast majority of O_2 moves through channels in RBC plasma membrane: AQP1, Rh_{Cx}, and at least one additional channel that is blocked by pCMBS. In other words, under our experimental conditions, "Overton's rule" applies, at most, to ~9% of the O_2 traffic across the murine RBC membrane.

Predicted effects of dKO/pCMBS on the kinetics of parameters related to intracellular O_2 and Hb

In Figure 4*A*-*F*, we examined the simulated time courses of six parameters for control (drug-free) WT RBCs: $[O_2]_i$, $[HbO_2]_i$, $[O_2]_i + [HbO_2]_i$, HbSat, $[Hb]_i$, and J_{M,O_2}. In Figure 7*A*-*F*, we extend this WT/Ctrl analysis (green curves) by simulating the slowest O_2 offloading protocol observed in paper #1[32]: a dKO RBC pre-treated with pCMBS (purple curves).

On the time scale of the main part of Figure 7*A*, the initial rates of decline for $[O_2]_i$ appear to be nearly the same for dKO/pCMBS and WT/Ctrl. The inset—a blow-up of the initial 1 ms of the simulation—shows that, in fact, the time course for dKO/pCMBS is much slower than for WT/Ctrl, reflecting a P_{M,O_2} that is reduced by ~91%.

For $[HbO_2]$ in Figure 7*B*, the time course of the decline for dKO/pCMBS is markedly slower than for WT/Ctrl.

The time courses of $[O_2]_i + [HbO_2]_i$ in Figure 7*C* are nearly the same as for $[HbO_2]$ alone in Figure 7*B* because, of the total O_2 in the RBC, ~98% is bound to Hb as HbO_2.

---

[31] See Paper #2>Results>Proteomics

[32] See Paper #1>figure 5*d*, light purple bar

The time courses of HbSat in Figure 7*D*, when appropriately scaled, are nearly the same as for $[HbO_2]_i$ in Figure 7*B* because $[HbO_2]_i$ is the numerator in the calculation of HbSat.

Because the sum $[Hb]_i + [HbO_2]_i$ is constant, the time courses of $[Hb]_i$ in Figure 7*E* is the inverse of $[HbO_2]_i$ in Figure 7*B*.

Finally, in Figure 7*F*, the transmembrane flux J_{M,O_2} is initially ~10-fold higher for WT/Ctrl than for dKO/pCMBS. For dKO/pCMBS, the J_{M,O_2} time course has a similar shape, but is scaled down by 91%, reflecting the reduced P_{M,O_2}.

Mathematical simulations exploring the predicted sensitivity of k_{HbO2} to eight key kinetic and geometric parameters

To understand better the dependence of O_2 offloading on a range of parameters in Table 1, we performed a sensitivity analysis, studying eight key parameters. See Figure 2 for an overview of the model. Our approach was to start with the parameter values in Table 1; that is, with the provisional value P_{M,O_2} = 0.15 cm s^{-1}, our simulation yields the provisional MMM-k_{HbO2} = 3.99 s^{-1}. Next, as described in the following five sub-sections, we computed k_{HbO2} as we systematically varied, one at a time, each of the following: $k_{HbO2 \rightarrow Hb+O2}$ in Figure 8, $[Hb_{Total}]_i$ in Figure 9, each of the four diffusion constants in Figure 10*A–D*, ℓ_{EUF} in Figure 11, and $Ø_{Sphere}$ in Figure 12.

In each of these figures or panels, we plot MMM-k_{HbO2} on the y-axis and the varied parameter (as a % of the standard parameter value) on the x-axis. Thus, when the standard value of the parameter = 100%, MMM-k_{HbO2} = 3.99 s^{-1}. As noted in our introduction of Figure 5, here we assume that all RBCs are intact BCDs, as for SC-k_{HbO2} values in paper #1.

In each figure/panel, we present eight dashed horizontal lines, one for each of the experimental conditions, each coded with a colored circle with same meaning as in Figure 6. For the y-axis value of a horizontal dashed line, we scale the hemolysis-corrected MMM-k_{HbO2} of 3.99

s^{-1} for the WT/Ctrl by the experimental condition's % decrease in SC-k_{HbO_2} vs. WT/Ctrl (Table 3, bottom line). Thus, MMM-k_{HbO_2} = 3.99 s^{-1} for WT/Ctrl (0% decrease) and falls to ~0.9 s^{-1} for dKO/pCMBS (78% decrease in MMM-k_{HbO_2}).

$k_{HbO_2 \rightarrow Hb+O_2}$ (governing reaction $HbO_2 \rightarrow Hb + O_2$)

Figure 8 shows the dependence of MMM-k_{HbO_2} on $k_{HbO_2 \rightarrow Hb+O_2}$. As $k_{HbO_2 \rightarrow Hb+O_2}$ rises, MMM-k_{HbO_2} rises at first rapidly and then more slowly. The red dot represents the provisional control condition (i.e., WT/Ctrl) in which $k_{HbO_2 \rightarrow Hb+O_2}$ is 100% of the standard parameter value (labeled in green on the x-axis) and MMM-k_{HbO_2} is the familiar hemolysis-corrected value of 3.99 s^{-1}. The condition with our smallest-observed % decrease in SC-k_{HbO_2} is AQP1-KO/Ctrl (i.e., ~9% lower than WT/Ctrl; Table 3). In order for a decrease in $k_{HbO_2 \rightarrow Hb+O_2}$, by itself, to account for the observed ~9% decrease in k_{HbO_2}, $k_{HbO_2 \rightarrow Hb+O_2}$ would have to fall by ~27% (i.e., x ≅ 73%; right downward dashed arrow). Our largest-observed % decrease in SC-k_{HbO_2} was ~78%, for dKO/pCMBS (see Table 3). In order for a decrease in $k_{HbO_2 \rightarrow Hb+O_2}$, by itself, to lower the observed SC-k_{HbO_2} by ~78% (violet point and its horizontal dashed line), $k_{HbO_2 \rightarrow Hb+O_2}$ would have to have fallen by ~92% (i.e., x ≅ 8%; left downward dashed arrow).

In fact, our largest-observed decrease in $k_{HbO_2 \rightarrow Hb+O_2}$ was ~10% (see Table 2), for dKO/Ctrl. We conclude that the sensitivity of MMM-k_{HbO_2} to decreases in $k_{HbO_2 \rightarrow Hb+O_2}$ is far too small have an appreciable impact on our O_2-offloading data.

$[Hb_{Total}]_i$

Figure 9 shows the dependence of MMM-k_{HbO_2} on $[Hb_{Total}]_i$. Starting from our lowest plotted value of x = 50% of the standard parameter value, increases in $[Hb_{Total}]_i$ cause MMM-k_{HbO_2} to fall at first steeply and then more shallowly. The reasons for this slowing of O_2 offloading are two-fold: (1) oxygen diffuses through the RBC far more slowly when bound to the large HbO_2

tetramer than when free as O_2 and (2) as $[Hb_{Total}]_i$ increases, total O_2 increases—although $[O_2]_i$ does not—meaning that more time is required to rid the cell of O_2.

In order to account for even our smallest-observed decrease in SC-k_{HbO_2}—that is, 9% (Table 3) in AQP1-KO/Ctrl—$[Hb_{Total}]_i$ would have to increase by 17% (i.e., x ≅ 117%; downward dashed arrow). In fact, in our genotype-specific comparisons (see Table 2), MCHC (analogous to $[Hb_{Total}]_i$) tended to fall in the KOs, with the greatest decrease being ~5% in the AQP1-KOs/Ctrl. Thus, by themselves these decreases in MCHC would have caused an increase, rather than the observed decrease in SC-k_{HbO_2}. However, as noted in paper #2[33], the decreases in MCHC were accompanied by increases in MCV, which have the opposite effect on SC-k_{HbO_2} (as we will see below[27]). Thus, the MCHC and MCV effects tend to cancel.

In our drug studies (see paper #2[34]), pCMBS in dKO cells produced a 2% decrease—again in the wrong direction to explain a decrease in SC-k_{HbO_2}. On the other hand, pCMBS in WT cells produced a 4.4% increase in MCHC. However, examination of Figure 9 shows that increasing—$[Hb_{Total}]_i$ by 4.4% (i.e., x = 104.4%) would have only a trivial effect on MMM-k_{HbO_2}.

Diffusion constants

Figure 10 shows the dependence of MMM-k_{HbO_2} on the four relevant diffusion constants, namely, D for extracellular O_2 (the only relevant extracellular solute), and the three intracellular diffusion constants for the components of the equilibrium $HbO_2 \rightleftharpoons Hb + O_2$.

---

[33] See Paper #2>table 4

[34] See Paper #2>table 6

Extracellular D_{O_2}. Figure 10*A* shows that, starting from our standard parameter value for extracellular D_{O_2} (i.e., 1.3313×10^{-5} cm^2 s^{-1}; see Table 1)—indicated by the red dot—decreasing $(D_{O_2})_o$ at first has little effect, and then causes MMM-k_{HbO2} to fall steeply. However, $(D_{O_2})_o$—which almost certainly does not vary substantially with genotype—would have to fall by ~34% (i.e., x ≅ 66%; right downward dashed arrow) to account for the fall in SC-k_{HbO2} in our AQP1-KO/Ctrl experiments, and by ~94% (i.e., x ≅ 6%; left downward dashed arrow) to account for the dKO/pCMBS data.

Because $(D_{O_2})_o$ governs the ability of O_2 to diffuse through the EUF, away from the membrane surface to the bECF—where $[O_2] = 0$ to mimic the annihilation of O_2 by sodium dithionite or $(Na^+)_2S_2O_4^{=}$ (NDT)—we are not surprised that MMM-k_{HbO2} approaches zero as $(D_{O_2})_o$ approaches zero. Thus, if $(D_{O_2})_o$ were zero, O_2 offloading would stop as soon as $[O_2]$ at the outer surface of the membrane rose to match $[O_2]_i$.

Note that our model does not explicitly take into account the diffusion of NDT from the bECF into the EUF. Although the diffusion constant for $S_2O_4^{=}$ is doubtlessly lower than that for O_2, $[S_2O_4^{=}]_{bECF}$ is ~71-fold greater than the initial $[O_2]_i$. Thus, we expect the EUF to be flooded with $S_2O_4^{=}$—to annihilate O_2 as it exits the RBC) very early in the physiological experiment. It is for this reason that others believe that ℓ_{EUF} is probably <1 μm (Huxley & Kutchai, 1981; Vandegriff & Olson, 1984*b*; Holland *et al.*, 1985), which, if true, means that $(D_{O_2})_o$ is even less impactful than indicated in Figure 10*A*.

Intracellular D_{O_2}. Figure 10*B* shows that the dependence of MMM-k_{HbO2} on $(D_{O_2})_i$ is similar to that of $(D_{O_2})_o$ in Figure 10*A*. In fact, starting from the red dot in Figure 10*B*, which represents our standard parameter value for intracellular D_{O_2} (i.e., 2.7745×10^{-6} cm^2 s^{-1}; see Table 1), decreasing $(D_{O_2})_i$ causes MMM-k_{HbO2} to fall somewhat less steeply than does decreasing $(D_{O_2})_o$ in panel *A*. Thus, $(D_{O_2})_i$—which again we regard as unlikely to change substantially with genotype—would need to fall by ~40% (i.e., x ≅ 60%; right downward dashed arrow) to account for the fall

in SC-k_{HbO2} in our AQP1-KO/Ctrl experiments, and by ~98% (i.e., x ≅ 2%; left downward dashed arrow) to account for the dKO/pCMBS data.

Note that, as noted in Methods[35], our choice of $(D_{O_2})_i$ is already, historically, a rather low value. If $(D_{O_2})_i$ is in fact greater than we estimated, then the red dot would slide further to the right (i.e., on an even flatter part of the curve, then the MMM-k_{HbO2} would be even less sensitive to changes in $(D_{O_2})_i$.

Intracellular D_{HbO_2}. Figure 10*C* shows that MMM-k_{HbO2} is nearly insensitive to changes in D_{HbO_2} until, starting at the red dot, this parameter falls to a tiny fraction of its standard parameter value (i.e., 6.07×10^{-8} cm^2 s^{-1} cm s^{-1}; see Table 1). The reason is that the diffusion constant of tetrameric HbO_2 is so low that—even though the concentration of HbO_2 is high—the movement of HbO_2 per se toward the membrane during O_2 offloading has little effect on O_2 delivery, and thus to MMM-k_{HbO2}. Of course, in Figure 9 we saw that decreases in $[Hb_{Total}]_i$ can greatly increase MMM-k_{HbO2}. The reason is that Hb acts as a near-stationary buffer that binds O_2 and nearly immobilizes it until O_2 release from HbO_2 permits the now-free O_2 to resume its net diffusion to the membrane or to the next unoccupied Hb. Thus, we expect genotype-dependent changes in D_{HbO_2} to have only miniscule effects on SC-k_{HbO2} until D_{HbO_2} becomes so small that HbO_2 approaches absolute immobility.

Intracellular D_{Hb}. Figure 10*D* shows that MMM-k_{HbO2} is even less sensitive to changes in D_{Hb} than to D_{HbO_2}. The reasons are: (1) The diffusion constant for the deoxygenated Hb tetramer (i.e., standard parameter value = 6.07×10^{-8} cm^2 s^{-1}; see Table 1) is nearly as low as it is for the fully oxygenated tetramer. And (2) Hb is moving away from the membrane during O_2 offloading.

[35] See Methods>Mathematical modeling and simulations>Parameter values

Thus, even if D_{Hb} were zero, the empty tetramers would pile up—at least mathematically—at the inner surface of the membrane, still maintaining a gradient for HbO_2 tetramers to diffuse toward the membrane. At $D_{Hb} = 0$, the small decrease in MMM-k_{HbO_2} would reflect absent diffusion of free Hb into the depth of the cytosol, and thus decreased formation of new HbO_2.

ℓ_{EUF}

Figure 11 shows that MMM-k_{HbO_2} has only weak dependence on ℓ_{EUF}. Starting at x = 100% of the standard parameter value (i.e., ℓ_{EUF} = 1 μm), decreasing ℓ_{EUF} to as low as 90% of control (i.e., 0.1 μm) could raise SC-k_{HbO_2} by <25%. Could an increase in ℓ_{EUF} account for our physiological data? By itself, a ~3× increase in ℓ_{EUF} would be needed to replicate the SC-k_{HbO_2} decrease that we see with AQP1-KO/Ctrl (see downward dashed arrow), and a ~20× increase would be needed to replicate the RhAG-KO. No amount of ℓ_{EUF} increase, alone, could account for our other physiological data.

$Ø_{Sphere}$

Theoretical dependence of k_{HbO_2} on $Ø_{Sphere}$. The main part of Figure 12 and its inset (with a greatly expanded y-axis) show that MMM-k_{HbO_2} is rather sensitive to changes in the diameter of the equivalent sphere because of the impact of O_2 diffusion distance. The tails of the downward arrows are at the intersections of the blue MMM-k_{HbO_2} curve and their respective observed SC-k_{HbO_2} values (i.e., horizontal dashed lines):

Arrow #1. Our largest $Ø_{Sphere}$ was for RhAG-KO/Ctrl, namely 2.18 μm (Table 2, data row 5), which is ~7.9% greater than the value of 2.02 μm for WT/Ctrl. According to the curve in Figure 12 (see leftmost downward arrow), the percent increase in $Ø_{Sphere}$ would have had to have been nearly 3× greater—about 20%—to account, by itself, for the observed decrease in SC-k_{HbO_2}.

Arrow #2. Our second largest computed $Ø_{Sphere}$ was for dKO/Ctrl, namely 2.14 μm (Table 2, data row 5), which is only ~5.9% greater than the WT/Ctrl value. According to our sensitivity analysis, the percent increase in $Ø_{Sphere}$ would have to have risen by nearly 7×—by somewhat more than 40% (i.e., x ≅ 142%; 2nd downward arrow)—in order to account for the observed decrease .

Recall that the analyses in Figure 5—which take into account not just $Ø_{Sphere}$ but all genotype-specific data—predict only a ~4% decrease for RhAG-KO/Ctrl (vs. observed ~17%), and a ~4% to ~6% decrease for dKO/Ctrl (vs. observed ~30%).

Arrows #3, #4, #5. At greater increases in $Ø_{Sphere}$, the curve flattens, so that one would have to invoke a ~100% increase (i.e., x ≅ 200%; 3rd downward arrow) to account for the dKO/DIDS data, more than a 140% increase (i.e., x > 240%; 4th downward arrow) to account for the WT/pCMBS data, and nearly a 300% increase (i.e., x > 394%; rightmost downward arrow) to account for the dKO/pCMBS results. All of these values are unrealistic. We conclude that, by themselves, changes in $Ø_{Sphere}$ cannot account for our physiological data.

Tendency of MCHC and MCV effects to cancel. As already noted, in RBCs from KO strains, MCHC (a surrogate for $[Hb_{Total}]_i$; see above[36]) tends to fall, thereby speeding O_2 offloading. On the other hand, as we just saw here, MCV (related to $Ø_{Sphere}$) tends to rise, thereby slowing O_2 offloading. These two effects tend to cancel, which is a reason that we see relative stability among the predicted MMM-k_{HbO_2} values among genotypes in Figure 5.

[36] See Results>Mathematical simulations exploring the predicted sensitivity …>$[Hb_{Total}]_i$

Accommodation for non-BCDs

The inputs to the MMM simulation include four observed experimental parameters: (1) MCV and (2) MCH (from which we compute MCHC), both of which come from automated hematology (paper #1[37]); (3) $Ø_{Major}$, from imaging flow cytometry (paper #2[38]); and (4) $k_{HbO2 \rightarrow Hb+O2}$, from stopped-flow absorbance spectroscopy on lysed RBCs (paper #1[39]). These values reflect all cells in the blood sample. An additional input is an estimate of P_{M,O_2}. The output of the simulation is k_{HbO2}. Because the blood comprises both the dominant biconcave disks and minority non-BCDs, the paired values P_{M,O_2} (input) and k_{HbO2} (output) represent hybrid values that to varying extents (depending on the sample) conflate BCDs and nBCDs. Our goal in this section is to obtain a (P_{M,O_2}, k_{HbO2}) pair that estimates as accurately as possible the values for BCDs.

Provisional estimates of P_{M,O_2} and MMM-k_{HbO2} (steps #13 and #14 & 14′ in Figure 1)

Table 4 is an expanded version of Table 3. The first two data rows of Table 4 lists the prevalences of BCDs and nBCDs from paper #2[40]; we consider these in the next sub-section.

As noted in Methods, we chose our provisional P_{M,O_2} for WT/Ctrl cells (Table 4, data row 3) to match the P_{M,CO_2} value of 0.15 cm s^{-1} that Endeward et al (Endeward *et al.*, 2006) obtained for the membrane CO_2 permeability of human RBCs. MMM simulations based on P_{M,O_2} = 0.15 cm s^{-1} yield a provisional MMM-k_{HbO2} of 3.99 s^{-1} (row 4), a value that is rather close to the highest

---

[37] See Paper #1>Results>Hematological and related parameters >Automated hematology

[38] See Paper #2>Results>Morphometry>Imaging flow cytometry

[39] See Paper #1>Results>Hematological and related parameters>Hb kinetics ($k_{HbO2 \rightarrow Hb+O2}$)

[40] See Paper #2>table 3

of the three shape-corrected stopped-flow values (i.e., ~4.09 s^{-1}; row 14 in Table 4) for three separate WT/Ctrl data sets that we employed in paper #1[41].

For the seven columns to the right of "WT/Ctrl" in Table 4, we chose the provisional P_{M,O_2} values in iterative processes in which each P_{M,O_2} generated a corresponding provisional MMM-k_{HbO2} that approximately matched the experimentally determined HC-k_{HbO2} value. Note that all (P_{M,O_2}, k_{HbO2}) pairs lie on the sigmoidal k_{HbO2} vs. log(P_{M,O_2}) curve in Figure 6.

nBCD prevalence (steps #15 & 15′ in Figure 1)

Recall that the first two data rows of Table 4 lists the prevalences of BCDs and nBCDs. The values for WT/Ctrl and dKO/Ctrl are around 2%, and may overestimate the actual values in SF experiments because of the extra time needed to prepare the samples for IFC analyses (compared to SF experiments; discussed in paper #2[42]). The nBCD prevalence values for the AQP1-KO/Ctrl and RhAG-KO/Ctrl groups are interpolations of the WT/Ctrl and dKO/Ctrl values. The nBCD prevalence values are ~6-fold higher for the WT/pCMBS cells than the corresponding WT/Ctrl cells. The dKO/pCMBS values are only ~2-fold greater than the corresponding dKO/Ctrl cells, probably reflecting the partial absence of pCMBS targets after the elimination of AQP1 and Rh_{Cx}. The largest nBCD prevalence comes with WT/DIDS cells, at ~41%; the figure falls to ~21% in the dKO/DIDS group. These large percentages probably reflect the long incubation with DIDS (1 hour), compounded—as noted above—by the extra time needed for executing the IFC studies.

---

[41] See Paper #1>Results>Mathematical simulations>Summary

[42] See Paper #2>Discussion>Morphometry>Imaging flow cytometry…>nBCD (poikilocyte) abundance >Time dependence

In the next four sections, we present a novel, 2-step approach for deconvoluting the HC-k_{HbO_2} data on a mixture of BCDs and nBCDs to extract an estimate of the k_{HbO_2} of BCDs, and thereby arrive at a P_{M,O_2} that we assume to apply to both BCDs and nBCDs.

First linear-combination analysis of k_{HbO_2} values (step #16 in Figure 1)

Using WT/Ctrl cells to illustrate our approach, we begin by making the (incorrect) assumption that the provisional MMM-k_{HbO_2} of ~3.99 s^{-1} (Table 4, row 4) represents only BCDs (note that row 5 repeats row 4). This allows us to construct an idealized time course of HbO_2 desaturation for BCDs (Figure 13*A*, green curve/furthest to the left). In parallel, knowing the measured $Ø_{Major}$ of nBCDs, and assuming them to be spheres with the same P_{M,O_2} as the BCDs (i.e., 0.15 cm s^{-1}), we construct another idealized desaturation time course, but this time for nBCDs (Figure 13*A*, blue curve/furthest to the right). We then linearly combine these two curves in proportion to the prevalence of their respective cells. Because the weighting is ~98.59% BCD (rows 5: LC-MMM-k_{HbO_2} = 3.99 s^{-1}) and 1.41% nBCD (rows 6: LC-MMM-k_{HbO_2} = 1.83 s^{-1}), the curve (Figure 13*A*, black) that describes the mixture of BCDs+nBCDs (rows 7: LC-MMM-k_{HbO_2} = 3.95 s^{-1}) lies barely to the right of the green BCD curve.

Figure 13*B* illustrates a similar analysis for dKO/pCMBS cells, at the opposite extreme of our experimentally observed spectrum of HC-k_{HbO_2} values (Table 4, rows 13–22). Here, reflecting the low P_{M,O_2}, all three curves show a slower offloading of O_2 from RBCs than in Figure 13*A*. Moreover, because the nBCD prevalence is ~4-fold higher than for the WT/Ctrl cells in Figure 13*A*, the separation between the green (BCDs) and black (mixture) is more discernable.

Rebalancing of k_{HbO_2} values (steps #17 & 17′ in Figure 1)

Recall that in row 7 of Table 4, k_{HbO_2} for the WT/Ctrl mixture is only ~3.95 s^{-1}, which is ~1% lower than our provisional estimate (~3.99 s^{-1}), yet much higher than the k_{HbO_2} for the nBCDs (1.83 s^{-1}). The goal of the present step is to rebalance the three k_{HbO_2} values so that the value for

the mixture matches the original provisional k_{HbO_2} as closely as possible. We make two assumptions:

- The term (MMM-$k_{HbO_2/Mixture}$ – MMM-$k_{HbO_2/BCDs}$)/(MMM-$k_{HbO_2/BCDs}$)) is maintained from the first linear combination throughout the rebalancing. That is, the rebalanced MMM-$k_{HbO_2/BCDs}$ exceeds the rebalanced MMM-$k_{HbO_2/Mixture}$ by the same fraction (~1.02% for WT/Ctrl) as it did during the first linear-combination step.
- The ratio (MMM-$k_{HbO_2/nBCDs}$)/(MMM-$k_{HbO_2/BCDs}$) remains similarly fixed from the first linear combination through the rebalancing. For WT/Ctrl, this is ~45.9%.

These provisos ensure that, after rebalancing, MMM-$k_{HbO_2/Mixture}$ is the same, within rounding errors, as our original provisional k_{HbO_2}, which, after all, really encompassed both BCDs and nBCDs. Thus, after rebalancing, MMM-$k_{HbO_2/BCDs}$ is slightly elevated (~4.04 s^{-1} for WT/Ctrl). Achieving this higher k_{HbO_2} requires that our corresponding rebalanced P_{M,O_2} be increased from the provisional value—our next step.

Rebalancing P_{M,O_2} values (steps #18 – #20 in Figure 1)

Armed with the rebalanced MMM-k_{HbO_2} (~4.04 s^{-1} for WT/Ctrl in Table 4, row 8), we compute the rebalanced P_{M,O_2} from an inverted/linearized version of Figure 6, shown in Figure 14. The result in the case of WT/Ctrl is a value (about "0.1546" cm s^{-1}) that is slightly higher than our provisional P_{M,O_2} of "0.1500" cm s^{-1}.

Shape-correction factor ($\mathcal{F}_{SC}$; steps #21 and #22 in Figure 1)

For a given data genotype/treatment, $\mathcal{F}_{SC}$ is the ratio (rebalanced MMM-k_{HbO_2})/(provisional MMM-k_{HbO_2}), ~1.0102 in the case of WT/Ctrl cells. Multiplying an HC-k_{HbO_2} value (~4.05 s^{-1} for the first set of WT/Ctrl data) by $\mathcal{F}_{SC}$ yields an estimate of SC-k_{HbO_2} (~4.09 s^{-1} in this example).

For dKO/pCMBS cells, with a higher nBCD prevalence than WT/Ctrl cells, $\mathcal{F}_{SC}$ is correspondingly higher, ~1.0376.

The remainder of Table 4, following the $\mathcal{F}_{SC}$ values, shows five pairs of reference values (HC-k_{HbO_2} and SC-k_{HbO_2}). The first set pertains to three data sets for control experiments: AQP1-KO/Ctrl, RhAG-KO/Ctrl, and dKO/Ctrl. The second set pertains to WT/pCMBS; the third, to WT/DIDS. The fourth and fifth sets are reference values for dKO/pCMBS and dKO/DIDS, respectively.

The last two rows of Table 4 show the percent decreases in HC-k_{HbO_2} and SC-k_{HbO_2}, based on shape-corrected values, for each genotype/treatment, relative to WT/Ctrl. These are the same values listed above in the bottom two rows of Table 3.

Discussion

To test whether the decreases in k_{HbO2} observed in paper #1 correspond to decreases in P_{M,O_2} and , if so, to provide estimates of P_{M,O_2} from measured k_{HbO2} values, we developed a three-dimensional reaction-diffusion model of O_2 efflux from an RBC. In this model, we simplify the RBC by assuming that it is a perfectly symmetric sphere, the diameter of which equals the computed thickness of an RBC. Note that the thickness of the biconcave disk near its edge (~2 μm)—not the major diameter (~6.8 μm for mice)—is the dimension of the RBC (when it is a BCD) that is critically important for gas exchange, as pointed out by several authors (Roughton, 1932; Ponder, 1948; Forster, 1964; Endeward, 2012). Our approach, which has the advantage of geometric (and thus computational) simplicity, ignores the dimpled center of the BCD, which contains relatively little hemoglobin.

Our macroscopic mathematical model describes how the concentrations of O_2, HbO_2 and Hb change in time and space, when O_2 diffuses out of the cytosol, across the plasma membrane, throughout the EUF and finally to the bECF. For our initial estimate of P_{M,O_2} in our mathematical simulations, we assume that P_{M,O_2} in mouse RBCs has the same value as measured by Endeward *et al.* (2006*b*) for the CO_2 permeability of human RBCs.

Even though our MMM model is relatively simple and based only on first principles, our assumptions as well as the physiological data that inform the model are sufficiently robust that our model makes physiologically meaningful predictions for a WT mouse. One strength of this study is the use of the genotype-specific flow-cytometry and hematology data that we generated in the two accompanying papers to establish internally consistent parameter values.

Krogh-Erlang Equation

In his pioneering modeling work on O_2 delivery from capillary to tissue, August Krogh (1919) introduced a now-famous equation—derived by his mathematician-colleague Mr. K

Erlang—that played a major role in elucidating the fundamental principles of how [O_2] changes both longitudinally along the capillary and radially away from it. This equation reflects a highly simplified view of the system, which of course was necessary at that time, given the limitations in available computational algorithms and computing power. The analysis by Kreuzer (1982) lists 15 assumptions—some of which he and others had noted previously—that are implicit in the derivation of the Krogh-Erlang equation. Assumption #12 states that "the diffusion coefficient [of O_2] is the same throughout the tissue." Assumption #7 (previously noted by Hess, 1930)—really a corollary of #12—states that "the capillary wall does not present any resistance to oxygen diffusion." Another corollary of #12 is that no cell membrane, including that of the RBC, offers resistance to O_2 diffusion. We examine implications of this implicit assumption in the section below.

How others concluded that the plasma membrane offers no resistance to O_2 diffusion

After Krogh's landmark paper, most practitioners in the RBC field adopted the aforementioned implicit assumption that membranes offer no resistance to O_2 diffusion. However, a series of studies from Roughton and his colleagues led to the suggestion that the plasma membrane of RBCs offers significant resistance to the movement of gases, including CO_2 and O_2 (Blank & Roughton, 1960; Gibson *et al.*, 1955; Forster, 1964; Roughton, 1964; Nicolson & Roughton, 1951; Lawson *et al.*, 1965). However, later studies questioned this possibility and attributed the observed resistance to the extracellular unconvected fluid layer[43] that surrounds the cells after flow stops in the SF apparatus (Kutchai, 1975; Coin & Olson, 1979; Huxley & Kutchai,

[43] We avoid using the classic term "unstirred layer" because it is defined operationally; it has meaning only in the steady state, in principle differs for each solute, and is not easily implemented in MMM (see Figure 2*A*).

1981; Vandegriff & Olson, 1984*b*; Holland *et al.*, 1985; Hughes & Bates, 2003). It is true that studies that focus on O_2 influx across RBCs are intrinsically challenging because this influx depletes O_2 at the surface of the RBC, and the EUF of that surrounds the RBC offers "resistance" to the replenishment of O_2 from the bECF (Coin & Olson, 1979; Huxley & Kutchai, 1981; Holland *et al.*, 1985; Hughes & Bates, 2003). Moreover, as pointed out by Vandegriff and Olson, the low solubility of O_2 in water enhances the effect of EUFs in experiments of O_2 influx (Vandegriff & Olson, 1984*b*). Nevertheless, it is possible that the implicit assumption of past authors—namely, that the plasma membrane offers no resistance of O_2 diffusion (i.e., R_{M,O_2}—or R_M for short—is 0)—may have led them to dismiss Roughton hypothesis prematurely. The total resistance (R_{Total}) to O_2 diffusion from its original location in the cytosol to bECF is the sum of the effective resistance of the intracellular fluid (R_{ICF}), R_M, and the resistance of the extracellular unconvected fluid (R_{EUF}). If one implicitly assumes that $R_M \cong 0$, then the sum ($R_M + R_{EUF}$) reduces to R_{EUF}, with the result that one computes erroneously high values for the EUF thickness. In the process, one concludes that the large EUF explains the experimental data without the need of invoking membrane resistance—a classic bootstrap maneuver.

Because Vandegriff and Olson recognized the challenge of studying O_2 influx, they investigated O_2 efflux. They reduced the effects of the EUF by adding large amounts of sodium dithionite (NDT) in the suspending medium (Vandegriff & Olson, 1984*b*). The NDT near the outer side of the plasma membrane annihilates the O_2 that has just left the RBC, thereby minimizing the build-up of O_2 and minimizing the EUF. Viewed somewhat differently, the NDT maximizes the outwardly directed O_2 gradient and therefore the rate of O_2 efflux (Holland *et al.*, 1985). Vandegriff and Olson used a reaction-diffusion model of an RBC, idealized as a cylindrical disk, to analyze the time course of their O_2 release data. They concluded that their mathematical model—which lacked a term analogous to R_M—could simulate their data without the need to include a membrane resistance to the movement of O_2. Instead, they accounted for their O_2-release data in the presence of NDT in the extracellular medium by including in the model an EUF, the width of which

increased with time from the initial value of 1 μm to ~30 μm (computed from an equation in ref. Holland *et al.*, 1985). In summary, because they implicitly assumed $R_M = 0$, these authors invoked a very large R_{EUF}, and used this result to conclude that $R_M \cong 0$.

It is worth noting that at least 3 sets of authors have performed physicochemical experiments in which they concluded that lipid mono/bilayers can offer substantial resistance to CO_2 or O_2 (Blank & Roughton, 1960; Strutwolf *et al.*, 2001; Ivanov *et al.*, 2004).

Recent observations on D_{O_2} in the cytosol of RBCs

In their 2020 paper, Richardson et al conclude that the D_{O_2} in the cytosol of RBCs is far lower than previously thought (Richardson *et al.*, 2020). The generally accepted value for D_{O_2} in RBC cytosol has been 5.09×10^{-6} cm^2/ s^{-1} at 10 °C (Clark *et al.*, 1985), which is ~38% of the value in water (i.e., 13.313×10^{-6} cm^2 s^{-1} at 10 °C). However, Richardson et al conclude that the actual D_{O_2} value in RBC cytosol is $<0.7 \times 10^{-6}$ cm^2 s^{-1} at 23 °C; we calculate that this value is < ~3.5% of the value in water at 23 °C (i.e., 20×10^{-6} cm^2 s^{-1}; see Han & Bartels, 1996). Thus, the D_{O_2} in cytoplasm predicted by Richardson et al should be 70/2000 = 1/29 of that in water.

Our calculation of the D_{O_2} of RBC cytosol (excluding membrane) at 10 °C. To apply the work of Richardson et al to our own, we must recompute their D_{O_2} for a temperature of 10 °C. If we divide the aforementioned figure of 13.313×10^{-6} cm^2 s^{-1} by 29, we arrive at a predicted value of D_{O_2} (based on the work of Richardson et al) of 0.45907×10^{-6} cm^2 s^{-1}. We are concerned that this D_{O_2} value is an underestimate because it is only ~10% of the previously accepted value, a point

recently made by Al-Samir *et al.* (2025). An inappropriately low estimate for $(D_{O_2})_i$ would impact us in two ways: (1) We would attribute to total diffusive resistance[44]

$$R_{\text{Total}} = R_{\text{ICF}} + R_{\text{M}} + R_{\text{EUF}}$$

an ICF component that in fact is due to a combination of both the membrane and EUF layer. (2) Our standard k_{HbO2} value for WT/Ctrl would fall from 3.99 s^{-1}—which comports very well with our physiological data—to only 2.61 s^{-1}. Therefore, we decided to compromise by averaging the Richardson value of 0.45907×10^{-6} cm^2 s^{-1} with the generally accepted value of 5.09×10^{-6} cm^2 s^{-1} (Clark *et al.*, 1985), and thereby arrive at a D_{O_2} in RBC cytoplasm of 2.7745×10^{-6} cm^2 s^{-1}.

Importance of values used in modeling

Thickness of EUF (ℓ_{EUF})

Several groups—Lawson *et al.* (1965), Coin and Olson (1979), Vandegriff and Olson (1984*b*), Yamaguchi *et al.* (1985), and Holland *et al.* (1985)—have emphasized the importance of employing a sufficiently high $[\text{NDT}]_o$ to minimize the EUF layer in stopped-flow experiments. Lawson *et al.* (1965) concluded that the final NDT after mixing must be at least 10 mM, although this low value was later challenged on the basis of the "packet model" used in their data analysis. Coin and Olson (1979) showed that the "packet model" greatly overestimated the power of NDT, and concluded (see their figure 9) that an NDT of 25 mM is required to maximize k_{HbO2}. Vandegriff and Olson (1984*b*) similarly discount the "packet model" and conclude that a final [NDT] of at

[44] Note that this equation includes all diffusive terms but does not include the reaction term for the dissociation of HbO_2

least 25 mM is required. Yamaguchi *et al.* (1985), used a final [NDT] of 40 mM to maximize k_{HbO_2}.

In preliminary work, we systematically reduced [NDT] and noted a small k_{HbO_2} falloff between $[NDT]_{Final}$ values of 25 and 20 mM, and progressively steeper declines below 20 mM. Therefore, we chose a final [NDT] of 25 mM. We note that commercial supplies of NDT are not reliable, and we routine discard the majority of NDT bottles because of infiltration of air and H_2O vapor (see paper #1[45]); NDT from such bottles routinely leads to lower k_{HbO_2} values.

Despite the use of NDT in our SF experiments—which virtually abolishes the EUF (Holland *et al.*, 1985)—in our mathematical model we make the conservative assumption that the EUF has a thickness of 1 μm and that no NDT is present in this layer. We simulate the annihilation of O_2 by NDT by assuming that the bECF contains no O_2 during the duration of the simulations. In Figure 11, we examine the dependence of k_{HbO2} on ℓ_{EUF}. When we increase ℓ_{EUF}, the simulated k_{HbO_2} asymptotically falls to a value that approximates the biological value that we observe with RBCs from an RhAG-KO/Ctrl mouse. Thus, no increase in ℓ_{EUF} can account for our data with RBCs from dKO mice, or RBCs treated with pCMBS or DIDS.

Lowering ℓ_{EUF} to values smaller than 1 μm causes steep increases in the simulated k_{HbO2} (i.e., decreases in the resistance of the EUF to O_2 diffusion, R_{EUF}). Starting from such elevated k_{HbO_2} values, the model can generate lower k_{HbO_2} values (e.g., 3.99 s^{-1}) by increasing R_M, that is, by decreasing the permeability of the plasma membrane to O_2 so that the sum ($R_{EUF} + R_M$) remains the same. In other words, if the EUF is thinner than 1 μm—which is likely to be the case in the

[45] See Paper #1>Discussion>Implications of the macroscopic mathematical model>Basic features of the model>Simulated k_{HbO_2} for WT/Ctrl RBCs

presence of high [NDT]—the membrane must make a greater contribution to the overall diffusive resistance of O_2.

Calculation of the contribution of the plasma membrane to total diffusive resistance to O_2

Let us assume that we can treat the diffusion of O_2 from the ICF of the RBC to the bECF like an electrical circuit (see Figure 2*A*), where, as in the preceding equation, R_{Total} is the sum $R_{ICF} + R_M + R_{EUF}$. In the next 3 sub-sections, we will compute each of the resistances on the right side of the equation, and then we will compute the fraction of R_{Total} that R_M represents. See Table 1 for parameter values used in simulations of RBCs from WT/Ctrl mice.

Calculate R_{ICF}. We start by computing—at the time t_{37} (i.e., 0.2503 s), when HbSat has fallen to 1/e of its initial value—the parallel fluxes of free O_2 (J_{O_2}) and HbO_2 (J_{HbO_2}) from the position of the average O_2 and HbO_2 molecules in the ICF. From these two fluxes, we then compute the total O_2 flux (J_{Total,O_2}).

First, we determine the number of O_2 molecules in each of the 101 shells (i = 1 to 101) that make up the model RBC, as well as the distance (ℓ) from the center of each shell to the inner surface of the plasma membrane (iM). For a WT cell with no inhibitors, we find that the average distance of an O_2 molecule from the iM is 2.792×10^{-5} cm. For HbO_2, a similar analysis yields an average distance of 2.560×10^{-5} cm. Because these distances are so similar, we used the average distance for O_2 and HbO_2, which is 2.68×10^{-5} cm, which corresponds to shell $i = k = 76$ from the center of the sphere. We call this average distance ℓ_k. Thus, the flux of free O_2 from ℓ_k to the iM is:

$$J_{O_2} = \frac{D_{O_2}}{\ell_k}\cdot\left([O_2]_k - [O_2]_{iM}\right) = 0.000540\ \mu\text{mole}/(\text{cm}^2\ \text{s}),$$

where D_{O_2} is the diffusion constant for O_2 in the ICF (see Table 1 for value), and where $[O_2]_k$ = 0.01528 mM and $[O_2]_{iM}$ = 0.01007 mM at t_{37}. For HbO_2,

$$J_{HbO_2} = \frac{D_{HbO_2}}{\ell_k} \cdot \left([HbO_2]_k - [HbO_2]_{iM}\right) = 0.000282 \text{ μmole} / (\text{cm}^2 \text{ s}),$$

where D_{HbO_2} is the diffusion constant for HbO_2 in the ICF (see Table 1 for value), and where $[HbO_2]_k$ = 6.869 mM and $[HbO_2]_{iM}$ = 6.744 mM at t_{37}.

Thus, the total O_2 flux from ℓ_k to the iM is

$$J_{Total,O_2} = J_{O_2} + J_{HbO_2} = 0.0008218 \text{ μmole} / (\text{cm}^2 \text{ s}).$$

The effective resistance to the diffusion of O_2 is[46]

$$R_{ICF} = \frac{\left([O_2]_k - [O_2]_{iPM}\right)}{J_{Total,O_2}} = \frac{\left(0.01528 \text{ mM} - 0.01007 \text{ mM}\right)}{0.0008218 \text{ μmole} / (\text{cm}^2 \text{ s})} \cong 6.334 \text{ s} \cdot \text{cm}^{-1}.$$

Calculate R_M. We calculate the resistance of the plasma membrane to O_2 diffusion as the reciprocal of the "true" microscopic permeability of the plasma membrane to O_2, which is 0.15 cm s^{-1} (see Table 1 for value). Thus,

$$R_M = \frac{1}{P_{M,O_2}} = \frac{1}{(0.15 \text{ cm s}^{-1})} = 6.666 \text{ s} \cdot \text{cm}^{-1}.$$

Calculate R_{EUF}. We calculate the resistance of the EUF to O_2 diffusion as

$$R_{EUF} = \frac{\ell_{EUF}}{(D_{O_2})_o} = \frac{(1.0 \times 10^{-4} \text{ cm})}{(1.3313 \times 10^{-5} \text{ cm}^2 \text{ s}^{-1})} = 7.511 \text{ s} \cdot \text{cm}^{-1},$$

---

[46] Apparent deviations in computed values are due to rounding errors

where ℓ_{EUF} is the thickness of the EUF and D_{O_2} is the diffusion constant for O_2 in the EUF (see Table 1 for values).

Compute the contribution of R_M to R_{Total}. We calculate the contribution of R_M to R_{Total} as

$$\text{Contribution of } R_M \text{ to } R_{Total} = \frac{R_M}{R_{Total}} = \frac{R_M}{R_{ICF} + R_M + R_{EUF}}$$
$$\frac{6.666\ \text{s}\cdot\text{cm}^{-1}}{6.334\ \text{s}\cdot\text{cm}^{-1} + 6.666\ \text{s}\cdot\text{cm}^{-1} + 7.511\ \text{s}\cdot\text{cm}^{-1}} = 32.5\%.$$

Note that if ℓ_{EUF} is in fact <1 μm (i.e., $R_{EUF} < 7.511$ s cm^{-1}), the contribution of R_M to total resistance would be greater than ~33%. Note also that if our compromise estimate for $(D_{O_2})_i$ is in fact too low (i.e., if we are overestimating R_{ICF}), this consideration would also increase the contribution of R_M to R_{Total}.

Potential contribution of channels to R_M and R_{Total}. In reaching the above conclusion that R_M represents at least ~33% of R_{Total} for WT/Ctrl RBCs under the conditions of our experiments, we did not consider inhibitors or KO strains. Our observed 30% decrease in SC-k_{HbO_2} caused by the dKO/Ctrl corresponds to a ~55% decrease in P_{M,O_2} (see Figure 6), so that R_M is now (6.666 s cm^{-1})/(1–0.55), which represents ~52% of R_{Total}. The 78% decrease in k_{HbO_2} caused by dKO/pCMBS corresponds to a ~91% decrease in P_{M,O_2}, so that R_M now rises to (6.666 s cm^{-1})/(0.55), so that R_M now is ~84% of R_{Total}—even with our conservative estimates of R_{ICF} (i.e., intracellular D_{O_2}) and R_{EUF} (i.e., ℓ_{EUF}). Viewed differently, for WT/Ctrl RBCs under the conditions of our experiments, the reason that R_M makes only a ~33% contribution to R_{Total} is that the O_2 channels make the membrane leaky.

It is not clear how drugs confined to the outside of the membrane or the genetic deletion of membrane proteins could produce the observed decreases of k_{HbO_2} in any way other than decreasing O_2 egress through protein channels. Moreover, an analysis of 8 key parameters (e.g., ℓ_{EUF}, cell

thickness) based on mathematical simulations shows that no reasonable change in any could explain our k_{HbO_2} data (Figure 8 through Figure 12).

Uniqueness of the sigmoidal k_{HbO2} vs. log(P_{M,O_2}) curve

Our development of the sigmoid curve in Figure 6 is novel. The curve describes all possible combinations of P_{M,O_2} and k_{HbO2} for a particular set of conditions. The detailed shape of the curve depends on experimental conditions (e.g., temperature) and MMM-simulation parameters (e.g., ℓ_{EUF}) as summarized in Table 1. Beyond these values, the shape of the sigmoid curve is potentially unique for each species or strain of animal—or individual humans with unique genetics and medical histories—because each will have a characteristic set of genotype-specific values for MCV and MCH (and thus MCHC), $Ø_{Major}$, and $k_{HbO2 \rightarrow Hb + O2}$ (see Table 2). Thus, with different experimental conditions and strains/species, we expect to see major differences in the maximal-possible k_{HbO2} at the far right of the curve, which represents a membrane made of a film of water.

Accommodation for nBCDs

Our accommodation for nBCDs is also novel, founded on our MMM-simulations with various algebraic manipulations, together with a meticulous set of collected data. For RBCs from our WT and KO strains—studied in the absence of drugs—the prevalence of nBCDs is small and thus the corrections are very minor. In the presence of pCMBS the corrections become larger, and for DIDS, still larger. The accuracy of the corrections likely increases as nBCD prevalence falls, and would improve with a more detailed knowledge of the surface-to-volume ratio.

Acknowledgements

We thank Jean-Pierre Cartron for the gift of RhAG-KO mice. We thank him and Gerolf Gros and for extremely helpful discussions at the outset of the project. We also thank Pawel Swietach for comments on an earlier version of the manuscript. We thank Seong-Ki Lee for developing an improved approach for genotyping the RhAG-KO mice. We thank systems analyst Dale Huffman for using MATLAB to generate some of the figures. The authors gratefully acknowledge Daniela Calvetti and Erkki Somersalo for having developed the engine of an earlier version of the CO_2/pH reaction-diffusion model of an oocyte, which in part served as the starting point for the RBC model. We thank Thomas Radford for organizing the husbandry of the mouse colonies; Gerald Babcock for his role as laboratory manager; James W. Jacobberger and Philip G. Woost of the CWRU Flow Cytometry and Imaging Microscopy Core (FCIMC) for their assistance with flow cytometry; and Daniela Schlatzer of the CWRU Center for Proteomics and Bioinformatics for their assistance with mass spectrometry. This work was supported by Office of Naval Research (ONR) grant N00014-11-1-0889, N00014-14-1-0716, and N00014-15-1-2060; a Multidisciplinary University Research Initiative (MURI) grant N00014-16-1-2535 from the DoD, NIH grant multi-scale modeling grant 5U01GM111251 (to WFB), and NIH grant R01HL160857 (to WFB). R.O. and the modeling were supported in part by NIH grant K01-DK107787. W.F.B. gratefully acknowledges the support of the Myers/Scarpa endowed chair.

Tables

Table 1. Parameter values used in mathematical simulations of control RBCs from WT mice *

		Bulk ECF	Plasma membrane	Bulk ICF	Reference
Physical constants					
Temperature (°C)		10		10	Paper #1
P_{H_2O}, Vapor pressure of H_2O (mmHg)				9.2	From Forstner & Gnaiger (1983)
Literature values					
P_{50}, P_{O_2} of half-maximal hemoglobin saturation curve (mmHg)				9.35	From Roughton *et al.* (1936)
O_2 solubility (mM/mmHg)				2.24×10^{-3}	From Forstner & Gnaiger (1983)
Hill coefficient				2.7	From ref. (Popel, 1989)
Assumptions					
P_{M,O_2}, O_2 permeability (cm/s)			0.15		Assumed same as CO_2 permeability in RBCs (Endeward *et al.*, 2006)
ℓ_{EUF}, Thickness of EUF (μm)		1.0			
Thickness of membrane (nm)			5		
Shell thickness (cm or μm)		10^{-6} or 10^{-2}		10^{-6} or 10^{-2}	
Calculated values					
$Ø_{Sphere}$, Sphere diameter (cm or μm)				2.02×10^{-4} or 2.02	See Methods
D, Diffusion coefficient ($cm^2\ s^{-1}$)	O_2	1.3313×10^{-5}			Computed using data from ref. (Han & Bartels, 1996)
				2.7745×10^{-6}	See Discussion

	Hb	0		6.07×10^{-8}	Computed using data from ref. (Clark *et al.*, 1985)
	HbO_2	0		6.07×10^{-8}	Computed using data from ref. (Clark *et al.*, 1985)
Hb/HbO_2 reaction Rate constants (s^{-1}) ($mM^{-1}\ s^{-1}$) Equilibrium constant (mM)	 $k_{HbO2 \rightarrow Hb+O2}$ † $k_{Hb+O2 \rightarrow HbO2}$ ‡ K			 11.60 6.7481×10^4 ($k_{Hb+O2 \rightarrow HbO2}$ varies with $[O_2]$; 1.1790×10^{-4} (K varies with $k_{Hb+O2 \rightarrow HbO2}$; this is initial value)	 Measured§ Computed using Eqn (4) in Methods Calculated as ($k_{HbO2 \rightarrow Hb+O2}/k_{Hb+O2 \rightarrow HbO2}$)
Concentration (mM)	Total Hb	0		18.73	See Methods
	O_2	0		0.3532 (21% O_2)	Computed from O_2 solubility (above), using Henry's law
	HbO_2 monomer	0		18.6767	Computed using the relation $[HbO_2] = [Hb]_{Total}\ ([O_2]^n/(K+[O_2]^n)$
	Hb monomer	0		0.0533 mM	Computed as $[Hb]_{Total} - [HbO_2]$

* Parameter values correspond to the experimental temperature of 10°C. Control refers to the absence of drugs.

† Corresponds to k in Eqn (2).

‡ Corresponds to k' in Eqn (2).

§ The value of 11.60 s^{-1} is the mean of 16 early $k_{HbO2 \rightarrow Hb+O2}$ values, N=4 on each of 4 genotypes. These 4×4=16 are a subset of the final dataset of N=6 on each genotype. See paper #1>figure 10

Table 2. Genotype-specific parameter values used in mathematical simulations of control RBCs in Figure 5

Parameter \ Mouse	WT	AQP1-KO	RhAG-KO	dKO	Reference
MCV (fl)	47.9	49.5	51.0	49.8	From paper #2>table 4
$Ø_{Major}$, major diameter of RBC (μm)	6.80	6.69	6.53	6.55	From paper #2>table 3 (We assume that $OD_{Torus} = Ø_{Major}$)
r_{Torus}, minor radius of torus (μm)	1.01	1.04	1.09	1.07	Computed from Eqn (5)
R_{Torus}, major radius of torus (μm)	2.39	2.31	2.18	2.21	$R_{Torus} = (OD_{Torus})/2 - r_{Torus}$ Torus volume (computed from r_{Torus} & R_{Torus}) = MCV
$Ø_{Sphere}$, diameter of equivalent sphere (μm)	2.02	2.08	2.18	2.14	$Ø_{Sphere} = 2 \times r_{Torus}$
MCH, mean corpuscular hemoglobin (pg)	14.4	14.1	14.7	14.5	From paper #2>table 4
MCHC, mean corpuscular hemoglobin concentration (g/dl)	30.1	28.6	28.7	29.4	From paper #2>table 4 MCHC = MCH/MCV
$[Hb_{M,Total}]_i$, total concentration of Hb monomers (mM)	18.73	17.71	17.87	18.16	See Methods > Mathematical modeling and simulations > Calculation of Hb content
Initial $[Hb_MO_2]_i$, concentration of O_2-bound monomers (mM)	18.6767	17.6596	17.8191	18.1083	Computed using the relation $[Hb_MO_2] = [Hb_{M,Total}]\ ([O_2]^n/(K+[O_2]^n)$
Initial $[Hb_M]_i$, concentration of O_2-free monomers (mM)	0.0533	0.0504	0.0509	0.0517	Computed as $[Hb_{M,Total}] - [Hb_MO_2]$

$k_{HbO_2 \rightarrow Hb+O_2}$	11.60	12.31	12.03	10.44	See paper #1>figure 10

*Values not listed here, but necessary for the mathematical simulations, are in Table 1, which also repeats four values in the "WT" column of this table (i.e., $Ø_{Sphere}$, $[Hb_{M,Total}]_i$, initial $[Hb_MO_2]_i$, Initial $[Hb_M]_i$). dKO, double knockout (i.e., genotype *Aqp1–/–Rhag–/–*). The parameters in Table 2 that establish the genotype-specific conditions for each simulation are: (1) the RBC thickness, which we compute from the measured $Ø_{Major}$ and MCV, and (2) the total Hb concentration, which we compute from measured MCV and MCH. Thus, the input parameters for the four simulations that mimic RBCs from WT, AQP1-KO, RhAG-KO and dKO mice are all the same (including P_{M,O_2}) with the exception of the RBC thickness and total Hb concentration, which are specific to each mouse genotype.

Table 3. Parameter values predicted by macroscopic mathematical model

Parameter \ Protocol	WT/ Ctrl	AQP1-KO/Ctrl	RhAG-KO/Ctrl	dKO/ Ctrl	WT/ pCMBS	WT/ DIDS	dKO/ pCMBS	dKO/ DIDS
SC-P_{M,O_2} (cm s^{-1})	0.1546	0.1213	0.0983	0.0693	0.0281	0.0673	0.0143	0.0376
SC-k_{HbO2} (s^{-1})	4.0358	3.6828	3.3582	2.7988	1.5282	2.7533	0.8687	1.8937
↓ SC-P_{M,O_2} vs. WT/Ctrl	0%	21.56%	36.43%	55.20%	81.80%	56.47%	90.72%	75.71%
↓ SC-k_{HbO2} vs. WT/Ctrl	0%	8.85%	16.53%	30.47%	61.24%	31.25%	77.70%	52.98%

The SC-P_{M,O_2} (via the MMM) yields the SC-k_{HbO2}.

Ctrl, control conditions (i.e., no DIDS or pCMBS); MMM, macroscopic mathematical model; SC, shape corrected.

Table 4. Detailed parameter values predicted by macroscopic mathematical modeling

Parameter \ Protocol	WT /Ctrl	AQP1-KO /Ctrl	RhAG-KO /Ctrl	dKO /Ctrl	WT /pCMBS	WT /DIDS	dKO /pCMBS	dKO /DIDS
BCD prevalence	98.59%	98.04%	98.04%	97.49%	91.29%	58.97%	94.28%	88.73%
nBCD prevalence	1.41%	1.96%	1.96%	2.51%	8.71%	41.03%	5.72%	21.27%
Provisional P_{M,O_2} (cm s^{-1})	0.15	0.1175	0.0957	0.0673	0.0261	0.0417	0.0137	0.0309
Provisional MMM-k_{HbO_2} (s^{-1})	3.9949	3.6338	3.3146	2.7560	1.4388	2.0356	0.8372	1.6367
1st LC-MMM-k_{HbO_2} (s^{-1}), BCDs	3.9949	3.6338	3.3146	2.7560	1.4388	2.0356	0.8372	1.6367
1st LC-MMM-k_{HbO_2} (s^{-1}), nBCDs	1.8331	1.7489	1.6262	1.4390	0.6923	0.9697	0.4234	0.8058
1st LC-MMM-k_{HbO_2} (s^{-1}), mixture	3.9545	3.5855	3.2715	2.7138	1.3547	1.5050	0.8069	1.4146
Rebalanced MMM-k_{HbO_2} (s^{-1}), BCDs	4.0358	3.6828	3.3582	2.7988	1.5282	2.7533	0.8687	1.8937
Rebalanced MMM-k_{HbO_2} (s^{-1}), nBCDs	1.8519	1.7725	1.6476	1.4614	0.7353	1.3116	0.4394	0.9324
2nd LC-MMM-k_{HbO_2} (s^{-1}), mixture	3.9949	3.6338	3.3146	2.7560	1.4388	2.0356	0.8372	1.6367
Rebalanced P_{M,O_2} (cm s^{-1}), all cells	0.1546	0.1213	0.0983	0.0693	0.0281	0.0673	0.0143	0.0376
$\mathcal{F}_{SC}$ (shape-correction factor)	1.0102	1.0135	1.0132	1.0155	1.0621	1.3526	1.0376	1.1570
HC-k_{HbO_2} (s^{-1}) from SF*	4.0457	3.6758	3.3670	2.7982	----	----	----	----
SC-k_{HbO_2} (s^{-1}) from SF*	4.0871	3.7253	3.4114	2.8417	----	----	----	----
HC-k_{HbO_2} (s^{-1}) from SF†	3.4197	----	----	----	1.2609	----	----	----
SC-k_{HbO_2} (s^{-1}) from SF†	3.4547	----	----	----	1.3392	----	----	----
HC-k_{HbO_2} (s^{-1}) from SF‡	3.2116	----	----	----	----	1.6491	----	----
SC-k_{HbO_2} (s^{-1}) from SF‡	3.2445	----	----	----	----	2.2306	----	----
HC-k_{HbO_2} (s^{-1}) from SF§	----	----	----	2.4779	----	----	----	1.4707
SC-k_{HbO_2} (s^{-1}) from SF§	----	----	----	2.5165	----	----	----	1.7017
HC-k_{HbO_2} (s^{-1}) from SF‖	----	----	----	2.5885	----	----	0.8126	----
SC-k_{HbO_2} (s^{-1}) from SF‖	----	----	----	2.6287	----	----	0.8432	----
↓ SC-P_{M,O_2} vs. WT/Ctrl	0%	21.56%	36.43%	55.20%	81.80%	56.47%	90.72%	75.71%
↓ SC-k_{HbO_2} vs. WT/Ctrl	0%	8.85%	16.53%	30.47%	61.24%	31.25%	77.70%#	52.98%¶

The “nBCD prevalence” values (from IFC) for AQP1-KO and RhAG-KO are interpolations of the WT/Ctrl and dKO/Ctrl values. The Provisional P_{M,O_2} (via the MMM) yields the Provisional MMM-k_{HbO_2}. The Rebalanced P_{M,O_2} yields the Rebalanced MMM-k_{HbO_2}. $\mathcal{F}_{SC}$ is the quotient of (Rebalanced MMM-k_{HbO_2})/(Provisional MMM-k_{HbO_2}) in the same column.
LC, linear combination; MMM, macroscopic mathematical model; HC, hemolysis corrected; SC, shape corrected; SF, stopped flow; Ctrl, control conditions (i.e., no DIDS or pCMBS).
*WT/Ctrl in this row is the reference value for AQP1-KO, RhAG-KO, dKO; †WT/Ctrl in this row is the reference value for WT/pCMBS; ‡WT/Ctrl in this row is the reference value for WT/DIDS; §dKO/Ctrl in this row is the reference value for dKO/DIDS; ‖dKO/Ctrl in this row is the reference value for dKO/pCMBS; ¶Computed from % decreases in SC-k_{HbO_2} for dKO/Ctrl vs. WT/Ctrl (i.e., 30.47%) and dKO/DIDS vs. matched dKO/Ctrl (i.e., 32.38%, not shown); #Computed from % decreases in SC-k_{HbO_2} for dKO/Ctrl vs. WT/Ctrl (i.e., 30.47%) and dKO/DIDS vs. matched dKO/Ctrl (i.e., 67.92%, not shown).

Figure Legends

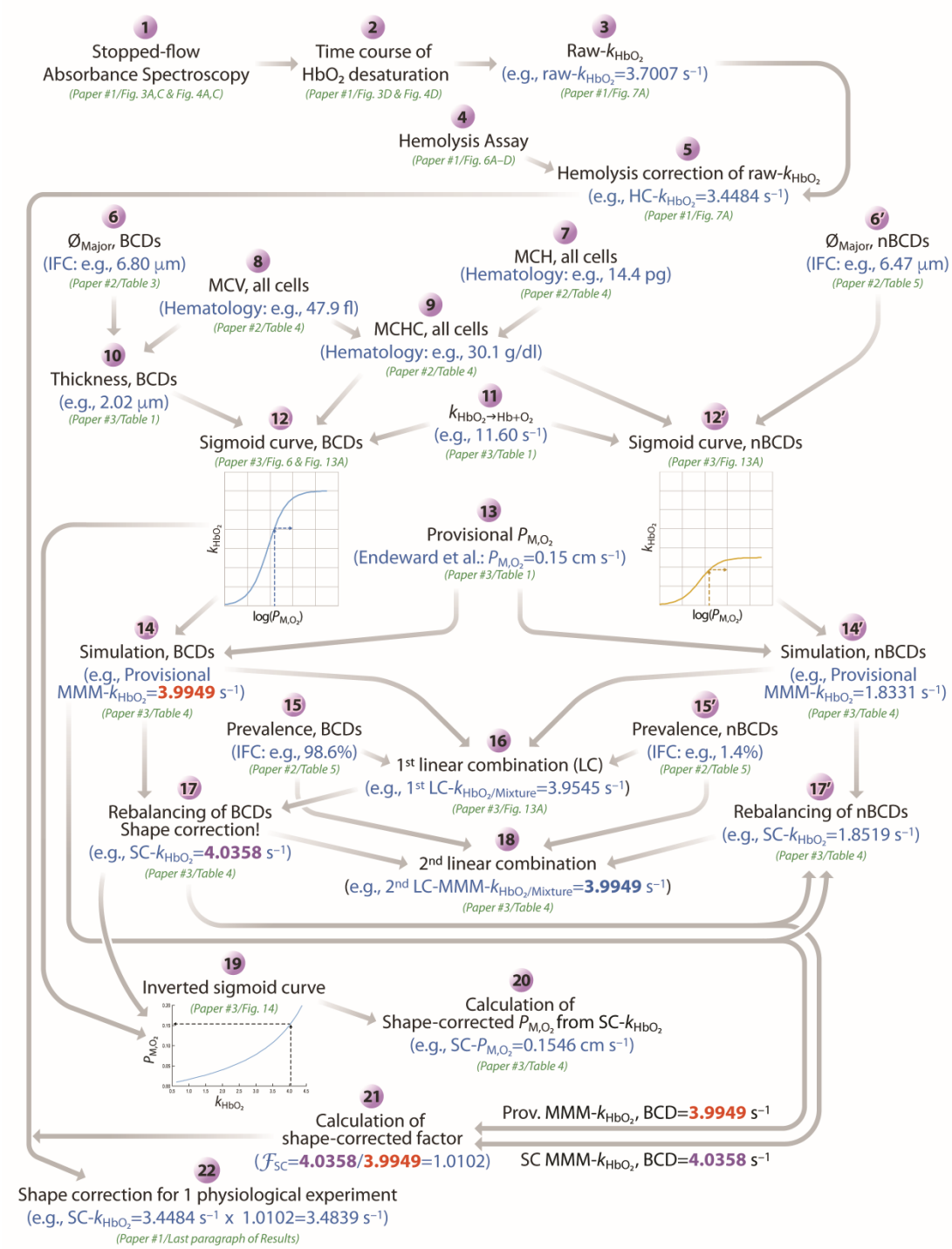

Figure 1. Workflow

The numerals 1 through 22 indicate the steps summarized in paper #1—and presented in detail, as

appropriate, in the present paper (paper #3), paper #1, or paper #2—to arrive, first, at a hemolysis-corrected (HC) k_{HbO_2} and, ultimately, at a shape-corrected (SC) k_{HbO_2}. At each step, we provide example values, if possible, and example figure/table numbers referenced to paper #1, paper #2, or the present paper.

We repeat workflow steps 1–5 for each mouse, ultimately arriving at an HC-k_{HbO_2} value for each. Step 6 applies to biconcave disks (BCDs), whereas step 6′ applies to non-biconcave disks (nBCDs). The same is true for steps 12 vs. 12′, 14 vs. 14′, 15 vs. 15′, and for 17 vs. 17′.

$\mathcal{F}_{SC}$, shape-correction factor; Hb, hemoglobin; IFC, imaging flow cytometry; MCH, mean corpuscular hemoglobin; k_{HbO_2}, rate constant for deoxygenation of HbO_2 within intact RBCs; $k_{HbO_2 \rightarrow Hb+O_2}$, rate constant for deoxygenation of HbO_2 in free solution; LC, linear combination; MCH, mean corpuscular hemoglobin; MCHC, mean corpuscular hemoglobin concentration; MCV, mean corpuscular volume; MMM-k_{HbO_2}, macroscopic mathematically modeled rate constant for deoxygenation of intracellular HbO_2; P_{M,O_2}, membrane permeability to O_2; Prov., provisional; $Ø_{Major}$, major diameter (of BCD or nBCD); SC-k_{HbO_2}, shape-corrected rate constant for deoxygenation of intracellular HbO_2.

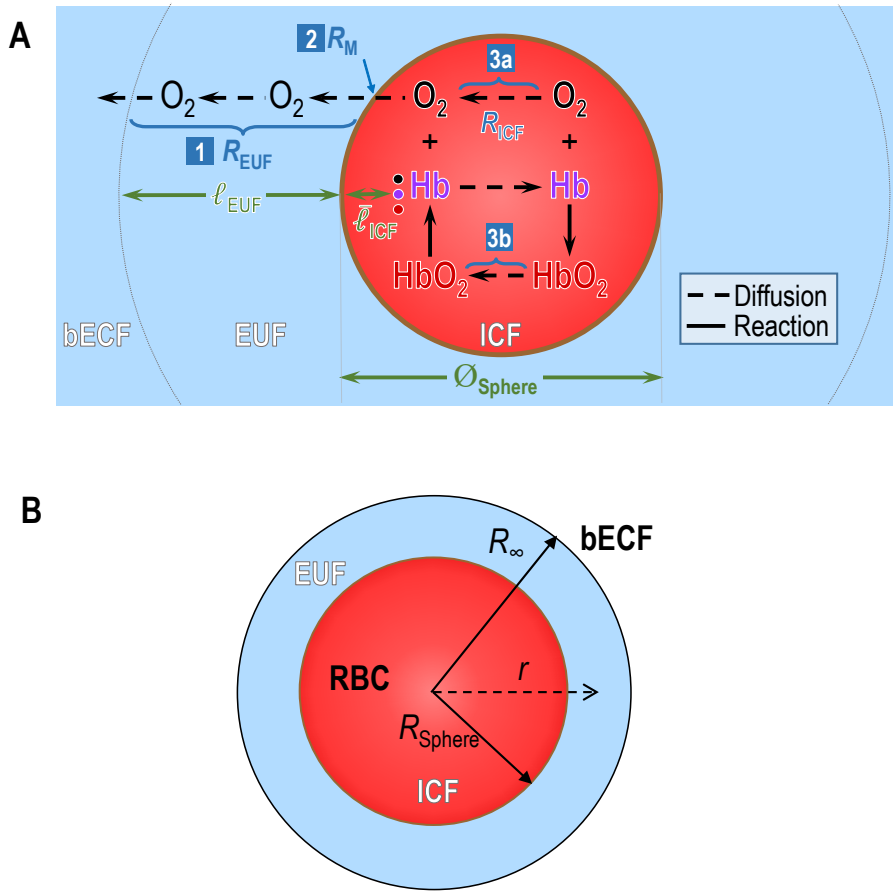

Figure 2. Mathematical model of O_2 efflux from an RBC

A, Major components of the mathematical model of spherical RBC cell, the diameter of which matches the computed thickness of an average RBC from a WT or KO mouse. See text for details on the model.

B, The computational domain.

For panel 'A', the abbreviations are: bECF, bulk extracellular fluid; EUF, extracellular unconvected fluid; ICF, intracellular fluid; M, plasma membrane; $Ø_{Sphere}$, diameter of sphere (matches thickness of RBC); ℓ_{EUF}, thickness of EUF; 3 values of $\bar{\ell}_{ICF}$ are average distance from M to the following 3 molecules in ICF: (a) O_2 (black dot and lettering), (b) Hb (violet), or HbO_2 (red) in ICF; [1] R_{EUF}, effective resistance offered by EUF to O_2 diffusion from M to bECF; [2] R_M, effective resistance offered by M to O_2 diffusion; [3] R_{ICF}, effective resistance offered by ICF to combined diffusion of O_2 and HbO_2. $1/R_{ICF} = 1/R_{ICFa} + 1/R_{ICFb}$, where R_{ICFa} is effective resistance offered by ICF to O_2 diffusion over the distance $\bar{\ell}_{ICF}$, from the position of the average O_2 to M; R_{ICFb} is effective resistance offered by ICF to HbO_2 diffusion over the distance $\bar{\ell}_{ICF}$, from the position of the average HbO_2 to M.

For panel 'B', the abbreviations are: R_∞, maximal radial distance from the center of the sphere ($R_\infty = R_{Sphere} + \ell_{EUF}$); r, radial distance from the center of the cell.

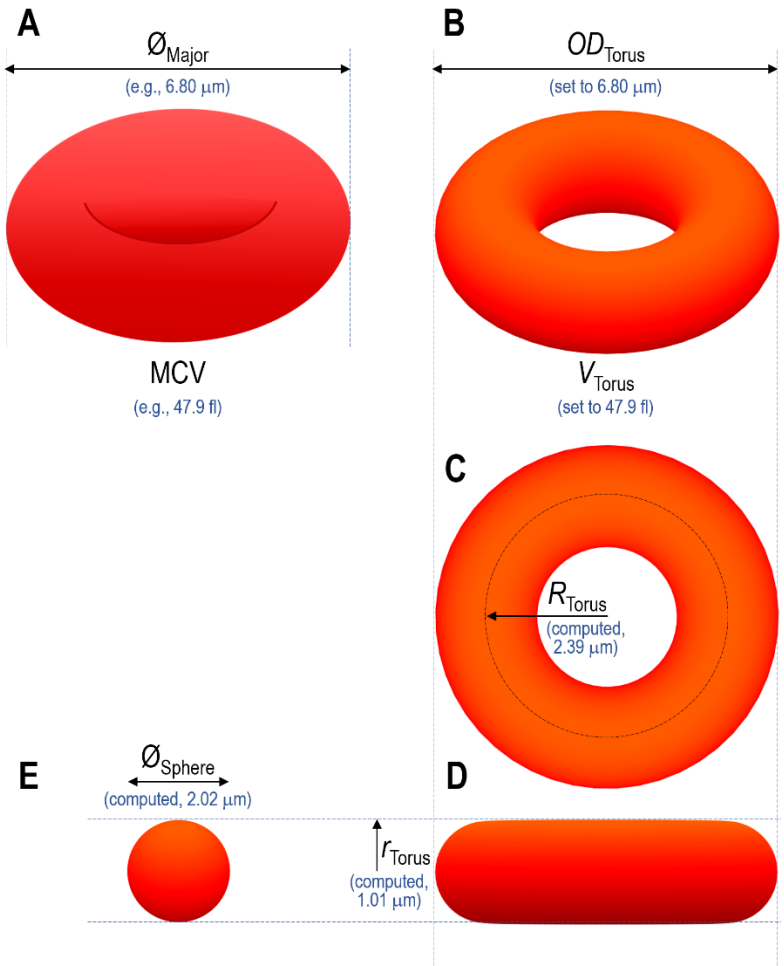

Figure 3. Conversion of biconcave disk geometry into torus geometry

A, Biconcave disk, tilted forward.

B, Torus, tilted forward.

C, Torus, top view.

D, Torus, side view.

E, Equivalent sphere.

$Ø_{Major}$, major diameter of biconcave disk; $Ø_{Sphere}$, diameter of equivalent sphere; MCV, mean corpuscular volume; OD_{Torus}, outer diameter of torus; r_{Torus}, minor radius of torus; R_{Torus}, major radius of torus; V_{Torus}, volume of torus (made equal to MCV).

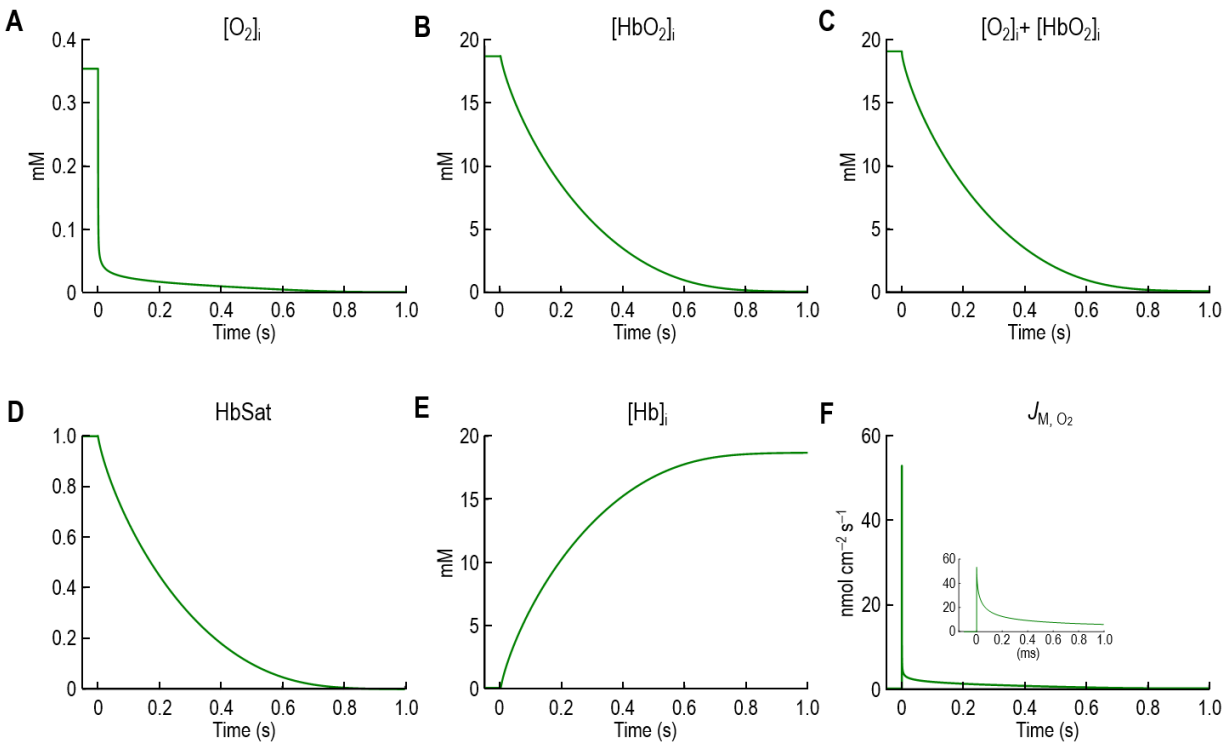

Figure 4. Simulated time courses of O_2/Hb-related parameters and transmembrane O_2 flux for cells mimicking WT/Ctrl (control/no inhibitors)

For this simulation, the input parameters are those reported in Table 1. See text for details on the model and simulations. All concentrations are in mM.

A, Concentration of free O_2, integrated over the entire volume of cytoplasm.

B, Concentration of oxyhemoglobin (HbO_2) monomers, integrated over the entire volume of cytoplasm.

C, Concentration of the sum of free O_2 and HbO_2 monomers, integrated over the entire volume of cytoplasm.

D, Hemoglobin saturation (HbSat), integrated over the entire volume of cytoplasm.

E, Concentration of free hemoglobin (Hb) monomers, integrated over the entire volume of cytoplasm.

F, Transmembrane O_2 flux (J_{M,O_2}). Note that the units are nmol cm^{-2} s^{-1} (rather than μmol cm^{-2} s^{-1}, as in the text of the Discussion). The inset shows a magnification of the first 1 ms of the simulated J_{M,O_2}

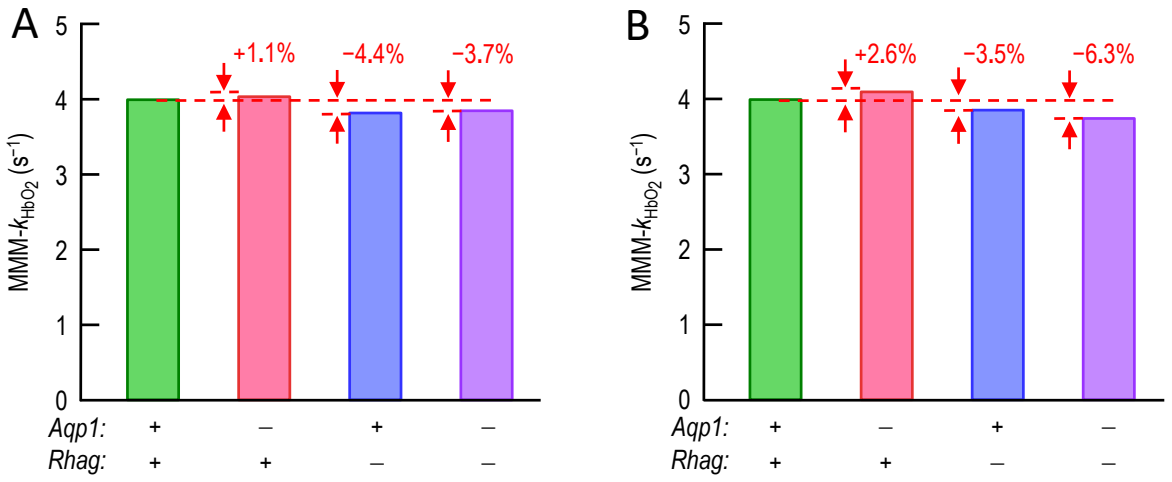

Figure 5. MMM-k_{HbO_2} values predicted from simulations of RBCs from WT and KO mice

Informed by hematological, morphological, and kinetic data, which provide genotype-specific information on MCV, MCH, $Ø_{Major}$, and $k_{HbO2 \rightarrow Hb+O2}$ (see Table 2) we perform four simulations, one per genotype, to test whether the collection of parameter changes can explain the physiologically observed decreases in shape-corrected (SC) k_{HbO2} values reported in figure 5*b* of paper #1: about –9% (AQP1-KO), –17% (RhAG-KO), and –30% (double KO). The values in red above each knockout bar indicate the % change predicted by MMM-k_{HbO2} vs. the observed change. Thus, the hematological/morphological changes cannot explain our observed k_{HbO2} data.

A, $k_{HbO2 \rightarrow Hb+O2}$ assumed to be 11.60 s^{-1} for all genotypes.

B, $k_{HbO2 \rightarrow Hb+O2}$ assumed to be specific for each genotype.

Except as noted otherwise, in these simulations we used the values summarized in Table 1, including P_{M,O_2} = 0.15 cm s^{-1}. We assume that all cells are intact (analogous to a hemolysis correction), and that all cells are biconcave disks (analogous to a shape correction). Thus, the two green bars have MMM-k_{HbO2} values of ~3.99 s^{-1}.

MMM-k_{HbO2}, macroscopic mathematically modeled rate constant for deoxygenation of intracellular HbO_2; *Aqp1*, the gene encoding murine aquaporin 1; *Rhag*, the gene encoding murine RhAG: +, gene present; –, gene deleted. MCV, mean corpuscular volume; MCH, mean corpuscular hemoglobin; $Ø_{Major}$, major diameter of biconcave disk; $k_{HbO2 \rightarrow Hb+O2}$, rate constant for deoxygenation of HbO_2 in free solution; P_{M,O_2}, membrane permeability to O_2.

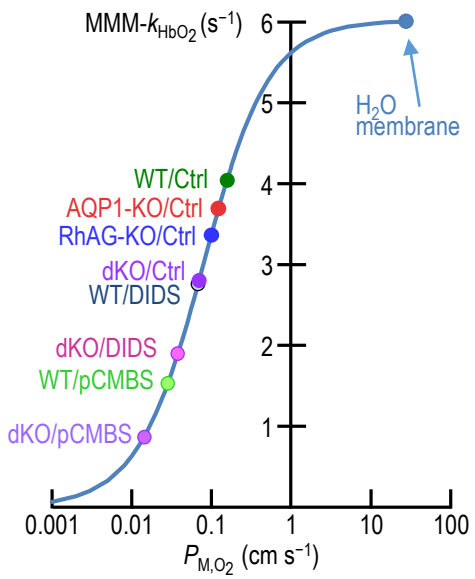

Figure 6. Predicted dependence of MMM-k_{HbO_2} on P_{M,O_2}

Using our macroscopic mathematical model (MMM), we systematically varied membrane O_2 permeability (P_{M,O_2}; logarithmic x-axis) to compute the corresponding rate constant for deoxygenation of HbO_2 (k_{HbO_2}; linear y-axis). Except for P_{M,O_2}, we used the values summarized in Table 1 for these 70^+ simulations. The resulting sigmoidal curve represents all possible combinations of P_{M,O_2} and k_{HbO_2} for $P_{M,O_2} > 0.001$ cm s^{-1}. The point labeled "H_2O membrane" is the result of a simulation in which we assumed that the diffusion constant of O_2 in the plasma membrane is the same as in water; it has the coordinates (P_{M,O_2} = 22.63 cm s^{-1}, k_{HbO2} = 5.9953 s^{-1}). The point labeled WT/Ctrl (i.e., RBCs from wild-type mice in the absence of drugs) has the coordinates (P_{M,O_2} = 0.1546 cm s^{-1}, k_{HbO_2} = 4.0358 s^{-1}), and represents the shape-corrected value obtained by the linear-combination procedure (steps #11 through #22 in Figure 1). The other labeled points also represent shape-corrected values, as summarized in Table 3. Note that the dKO/Ctrl and the WT/DIDS points nearly overlie each other.

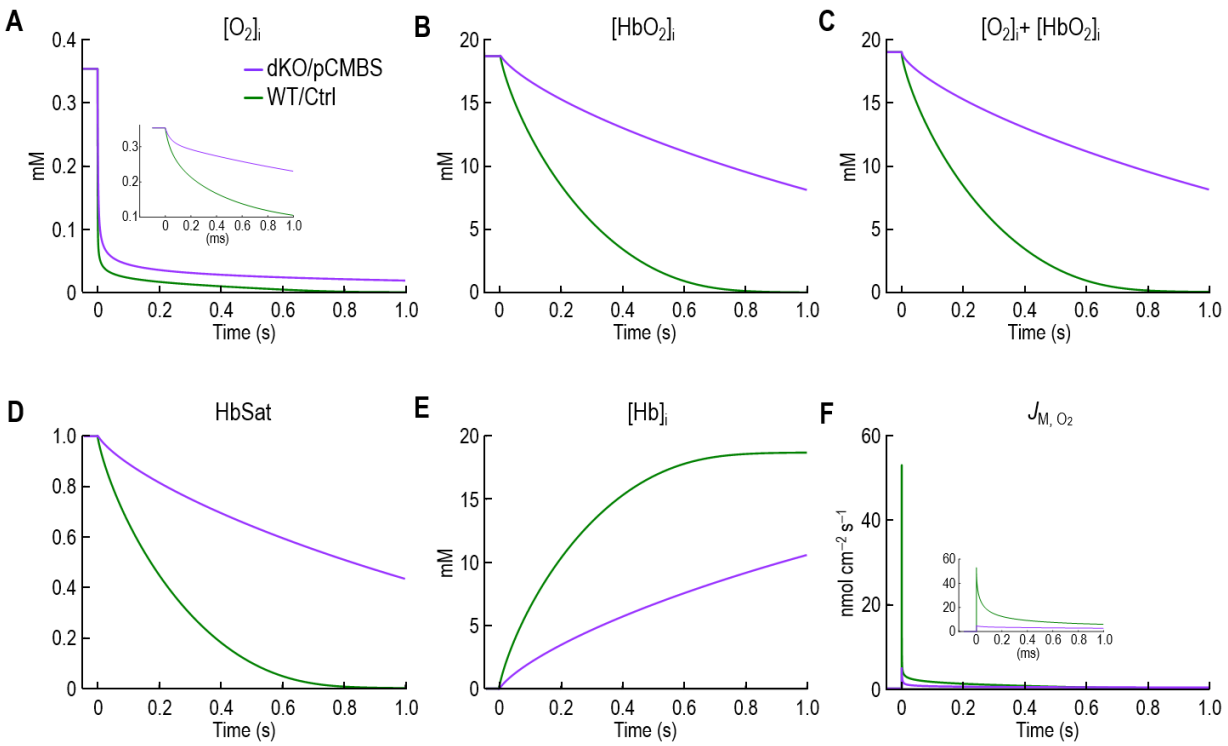

Figure 7. Simulated time courses of O_2/Hb-related parameters and transmembrane O_2 flux for cells mimicking WT/Ctrl (control/no inhibitors) vs. dKO/pCMBS

We extend the analysis of the WT/Ctrl condition (untreated RBCs from wild-type mice; green curves) shown in Figure 4 by adding the simulations of the slowest O_2-offloading protocol observed in paper #1 (i.e., figure 5*b*, light purple bar): the dKO/pCMBS condition (i.e., RBCs pre-treated with pCMBS; purple curves). For the WT/Ctrl simulation, the input parameters are those reported in Table 1. For the dKO/pCMBS simulation, the input parameters are the same, with the exception of P_{M,O_2} = 0.01365 cm s^{-1}. See text for details on the model and simulations. All concentrations are in mM.

A, Concentration of free O_2, integrated over the entire volume of cytoplasm. The inset shows a magnification of the first 1 ms of the simulated $[O_2]_i$.

B, Concentration of oxyhemoglobin (HbO_2) monomers, integrated over the entire volume of cytoplasm.

C, Concentration of the sum of free O_2 and HbO_2 monomer, integrated over the entire volume of cytoplasm.

D, Hemoglobin saturation (HbSat) integrated over the entire volume of cytoplasm.

E, Concentration of free hemoglobin (Hb), integrated over the entire volume of cytoplasm.

F, Transmembrane O_2 flux (J_{M,O_2}). Note that the units are nmol cm^{-2} s^{-1} (rather than μmol cm^{-2} s^{-1}, as in the text of the Discussion). The inset shows a magnification of the first 1 ms of the simulated J_{M,O_2}

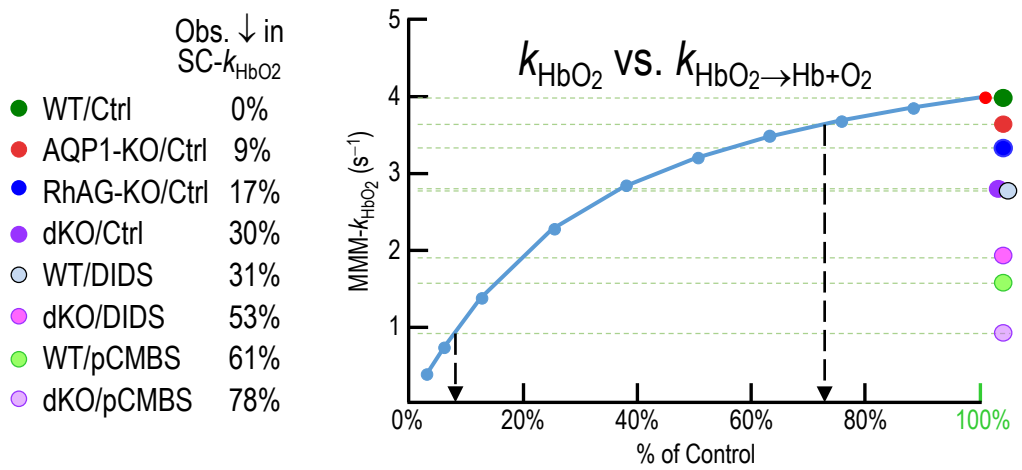

Figure 8. Mathematical simulations exploring the predicted sensitivity of k_{HbO_2} to changes in the rate constant of the reaction $HbO_2 \rightarrow Hb + O_2$.

Using our macroscopic mathematical model (MMM), we systematically varied the rate constant for deoxygenation of HbO_2 in free solutions: $HbO_2 \rightarrow Hb + O_2$ ($k_{HbO2 \rightarrow Hb+O2}$) to compute the corresponding the rate constant for deoxygenation of HbO_2 in intact RBCs (k_{HbO_2}). We computed the MMM-k_{HbO2} corresponding to the red dot—which corresponds to 100% of our standard $k_{HbO2 \rightarrow Hb+O2}$—by using the parameter values that come from Table 1. This is our standard condition for RBCs from wild-type mice in the absence of drugs (WT/Ctrl), and also is represented by the dark green circle and associated horizontal dashed green line. We performed nine additional simulations (blue dots) by decreasing $k_{HbO2 \rightarrow Hb+O2}$ by the indicated percentages, keeping all other parameter values constant. The seven other colored circles and associated horizontal dashed lines indicate the MMM-k_{HbO2} values, relative to WT/Ctrl, for each of the other 7 experimental conditions. As summarized in the legend on the left, for each condition, we multiplied the standard MMM-k_{HbO_2} (i.e., 3.99 s^{-1}) by the shape-corrected decrease in the experimentally observed k_{HbO_2} (e.g., ~9% for AQP1-KO/Ctrl cells) to obtain the y-axis coordinate for that condition (e.g., 3.64 s^{-1} for AQP1-KO/Ctrl). These % decreases are also listed in the last row of Table 3. The left downward arrow (tail on dKO/pCMBS) indicates the % decrease necessary to account for the effect of this condition on MMM-k_{HbO_2}. The right downward arrow is the same for AQP1-KO/Ctrl.

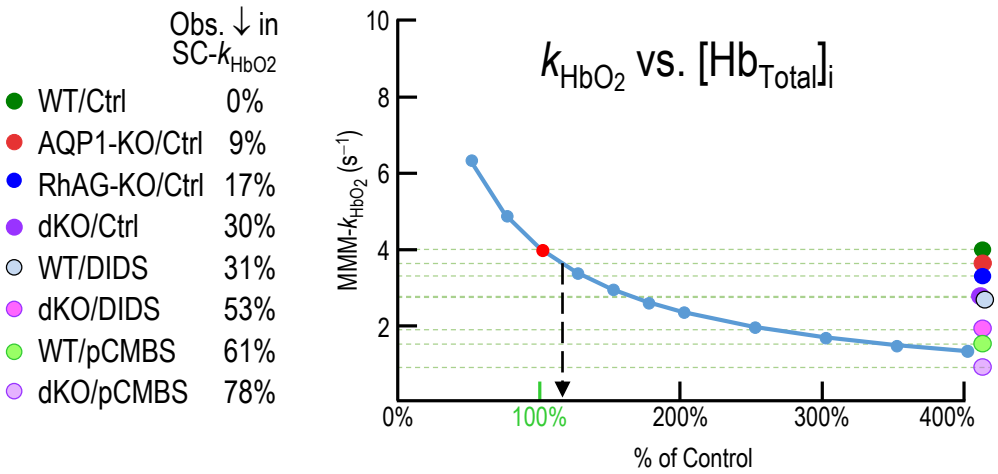

Figure 9. Mathematical simulations exploring the predicted sensitivity of k_{HbO_2} to changes in the total intracellular Hb concentration

Using our macroscopic mathematical model (MMM), we systematically varied the total intracellular Hb concentration, $[Hb_{Total}]_i$, to compute the corresponding rate constant for deoxygenation of HbO_2 in intact RBCs (k_{HbO_2}). We computed the MMM-k_{HbO2} corresponding to the red dot—which corresponds to 100% of our standard $[Hb_{Total}]_i$—by using the parameter values that come from Table 1. This is our standard condition for RBCs from wild-type mice in the absence of drugs (WT/Ctrl), and also is represented by the dark green circle and associated horizontal dashed green line. We performed ten additional simulations (blue dots) by decreasing $[Hb_{Total}]_i$ by the indicated percentages, keeping all other parameter values constant. The seven other colored circles and associated horizontal dashed lines indicate the MMM-k_{HbO2} values, relative to WT/Ctrl, for each of the other 7 experimental conditions. As summarized in the legend on the left, for each condition, we multiplied the standard MMM-k_{HbO_2} (i.e., 3.99 s^{-1}) by the shape-corrected decrease in the experimentally observed k_{HbO_2} (e.g., ~9% for AQP1-KO/Ctrl cells) to obtain the y-axis coordinate for that condition (e.g., 3.64 s^{-1} for AQP1-KO/Ctrl). These % decreases are also listed in the last row of Table 3. The downward arrow (tail on AQP1-KO/Ctrl) indicates the % decrease necessary to account for the effect of this condition on MMM-k_{HbO2}.

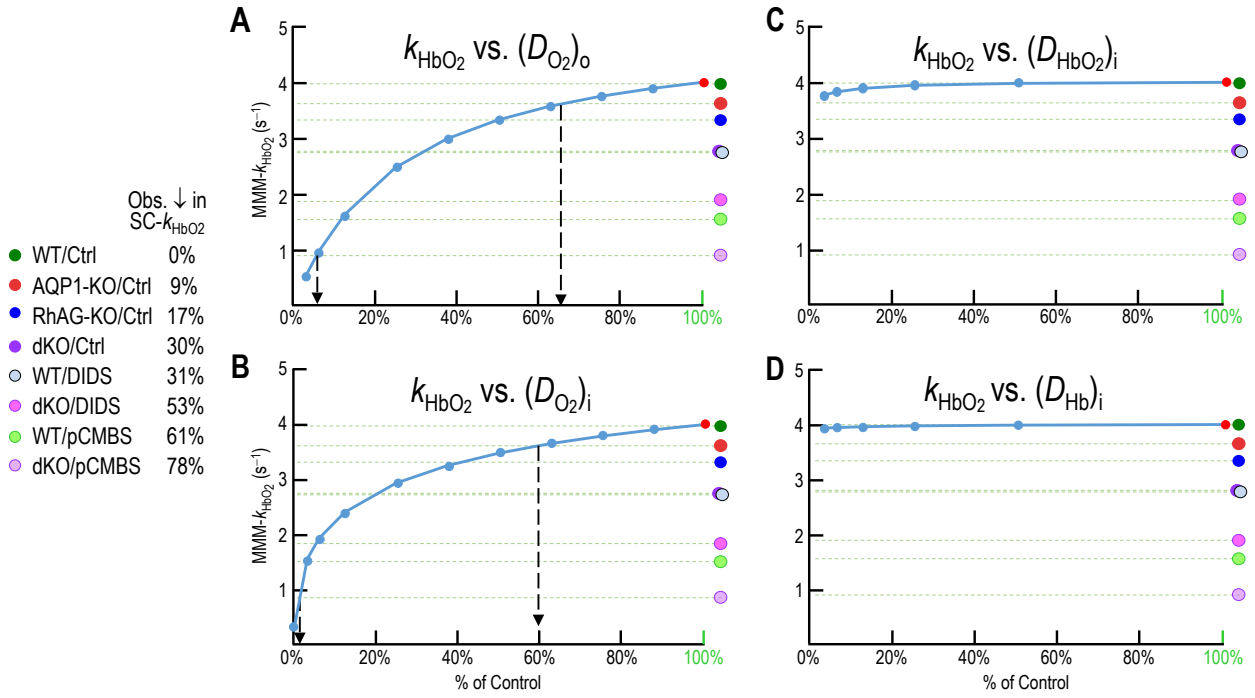

Figure 10. Mathematical simulations exploring the predicted sensitivity of k_{HbO_2} to changes in diffusion constants of solutes

Using our macroscopic mathematical model (MMM), we systematically varied the four relevant diffusion constants (D), one at a time, to compute the corresponding rate constant for deoxygenation of HbO_2 in intact RBCs (k_{HbO_2}). These four diffusion constants are: D for extracellular O_2—$(D_{O_2})_o$ in panel *A*; and the three intracellular diffusion constants for the components of the equilibrium $HbO_2 \rightleftharpoons Hb + O_2$, namely, $(D_{O_2})_i$ in panel *B*, $(D_{HbO_2})_i$ in panel C, and $(D_{Hb})_i$ in panel *D*.

We computed the MMM-k_{HbO2} corresponding to the red dot—which corresponds to 100% of the value of the varied parameter—by using the parameter values that come from Table 1. This is our standard condition for RBCs from wild-type mice in the absence of drugs (WT/Ctrl), and also is represented by the dark green circle and associated horizontal dashed green line. We performed additional simulations (blue dots) by decreasing the varied parameter by the indicated percentages, keeping all other parameter values constant. The seven other colored circles and associated horizontal dashed lines indicate the MMM-k_{HbO2} values, relative to WT/Ctrl, for each of the other 7 experimental conditions. As summarized in the legend on the left, for each condition, we multiplied the standard MMM-k_{HbO_2} (i.e., 3.99 s^{-1}) by the shape-corrected decrease in the experimentally observed k_{HbO_2} (e.g., ~9% for AQP1-KO/Ctrl cells) to obtain the y-axis coordinate for that condition (e.g., 3.64 s^{-1} for AQP1-KO/Ctrl). These % decreases are also listed in the last row of Table 3. The downward arrows (tails on AQP1-KO/Ctrl) indicates the % decrease necessary to account for the effect of the respective condition on MMM-k_{HbO2}.

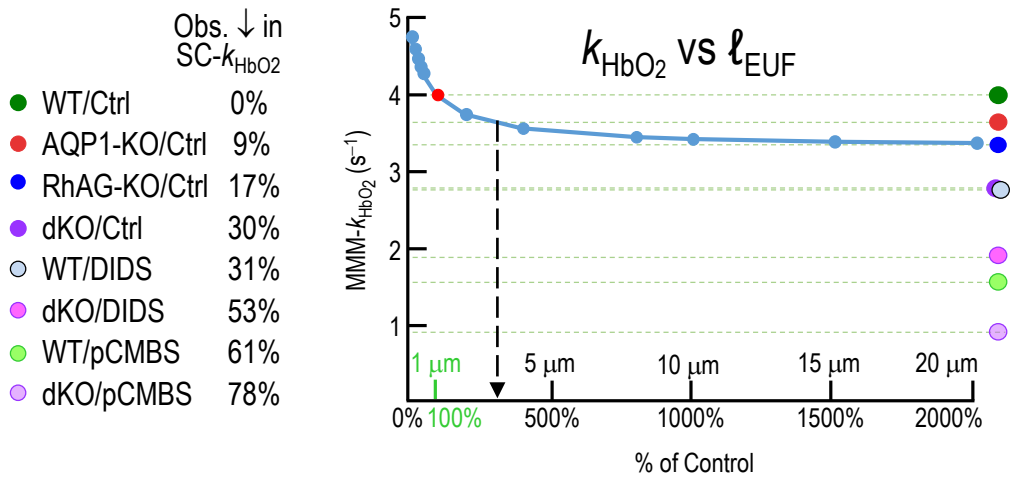

Figure 11. Mathematical simulations exploring the predicted sensitivity of k_{HbO_2} to changes in thickness of the EUF

Using our macroscopic mathematical model (MMM), we systematically varied the thickness of the EUF, ℓ_{EUF}, to compute the corresponding rate constant for deoxygenation of HbO_2 in intact RBCs (k_{HbO_2}). We computed the MMM-k_{HbO2} corresponding to the red dot—which corresponds to 100% of our standard ℓ_{EUF}—by using the parameter values that come from Table 1. This is our standard condition for RBCs from wild-type mice in the absence of drugs (WT/Ctrl), and also is represented by the dark green circle and associated horizontal dashed green line. We performed eleven additional simulations (blue dots) by decreasing ℓ_{EUF} by the indicated percentages, keeping all other parameter values constant. The seven other colored circles and associated horizontal dashed lines indicate the MMM-k_{HbO2} values, relative to WT/Ctrl, for each of the other 7 experimental conditions. As summarized in the legend on the left, for each condition, we multiplied the standard MMM-k_{HbO_2} (i.e., 3.99 s^{-1}) by the shape-corrected decrease in the experimentally observed k_{HbO_2} (e.g., ~9% for AQP1-KO/Ctrl cells) to obtain the y-axis coordinate for that condition (e.g., 3.64 s^{-1} for AQP1-KO/Ctrl). These % decreases are also listed in the last row of Table 3. The downward arrow (tail on AQP1-KO/Ctrl) indicates the % decrease necessary to account for the effect of this condition on MMM-k_{HbO2}.

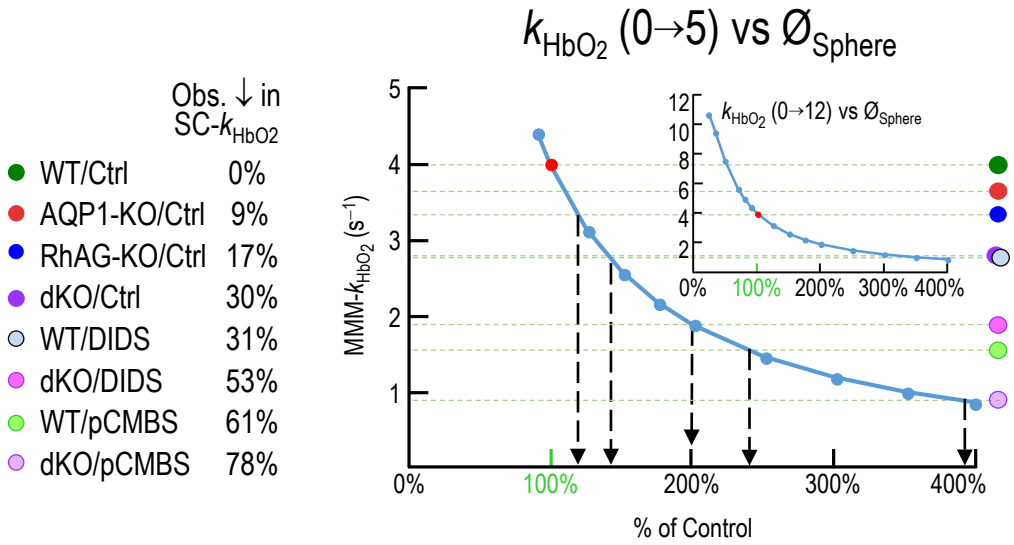

Figure 12. Mathematical simulations exploring the predicted sensitivity of k_{HbO_2} to changes in sphere diameter

Using our macroscopic mathematical model (MMM), we systematically varied the diameter of the sphere, Ø$_{Sphere}$, to compute the corresponding rate constant for deoxygenation of HbO_2 in intact RBCs (k_{HbO_2}). We computed the MMM-k_{HbO2} corresponding to the red dot—which corresponds to 100% of our standard Ø$_{Sphere}$—by using the parameter values that come from Table 1. This is our standard condition for RBCs from wild-type mice in the absence of drugs (WT/Ctrl), and also is represented by the dark green circle and associated horizontal dashed green line. We performed additional simulations (blue dots) by decreasing Ø$_{Sphere}$ by the indicated percentages, keeping all other parameter values constant. The seven other colored circles and associated horizontal dashed lines indicate the MMM-k_{HbO2} values, relative to WT/Ctrl, for each of the other 7 experimental conditions. As summarized in the legend on the left, for each condition, we multiplied the standard MMM-k_{HbO_2} (i.e., 3.99 s^{-1}) by the shape-corrected decrease in the experimentally observed k_{HbO_2} (e.g., ~9% for AQP1-KO/Ctrl cells) to obtain the y-axis coordinate for that condition (e.g., 3.64 s^{-1} for AQP1-KO/Ctrl). These % decreases are also listed in the last row of Table 3. Note that main panel shows the y-axis from 0 to 5 s^{-1}, whereas the inset expands the y-axis to extend from 0 to 12 s^{-1}. The downward arrows (tails on AQP1-KO/Ctrl, etc.) indicate the % decreases necessary to account for the effect of the respective condition on MMM-k_{HbO2}.

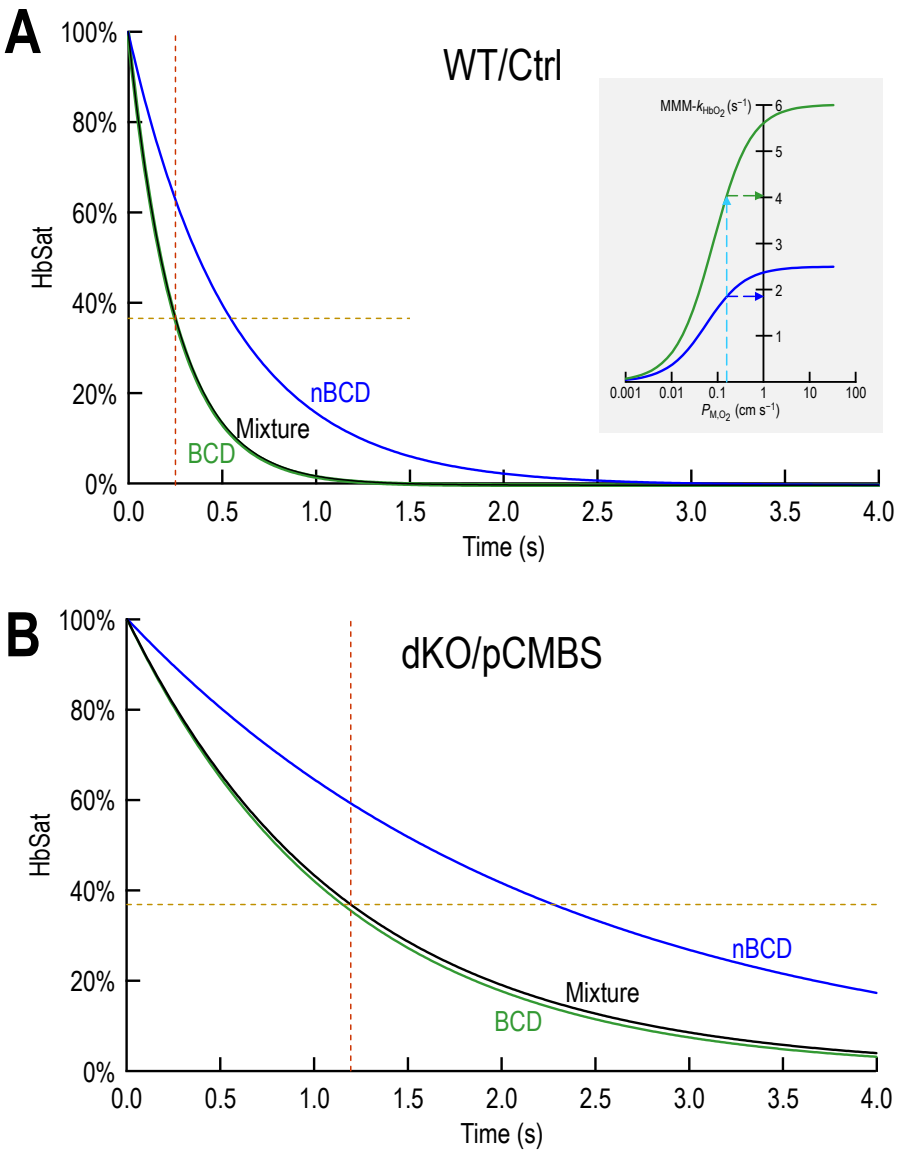

Figure 13. First linear-combination analysis of the rate constant for deoxygenation of HbO_2, k_{HbO_2}

A, WT/Ctrl. The green curve is the computed decay of HbSat (hemoglobin saturation) for a biconcave disk (BCD). The blue curve is the computed decay for a non-BCD. The two sigmoid curves in the inset illustrate how, given a value for P_{M,O_2}, we compute the corresponding MMM-HbO_2. The black curve, barely visible to the right of the green curve, is the linear combination of the green and blue curves, weighted for the respective prevalences of BCDs and nBCDs, respectively. The horizontal dashed curve represents the value of HbSat after 1 time constant for the mixture. The vertical dashed curve represents the corresponding time.

B, dKO/pCMBS. Similar to panel *A* except here the calculations are for a dKO cell treated with pCMBS.

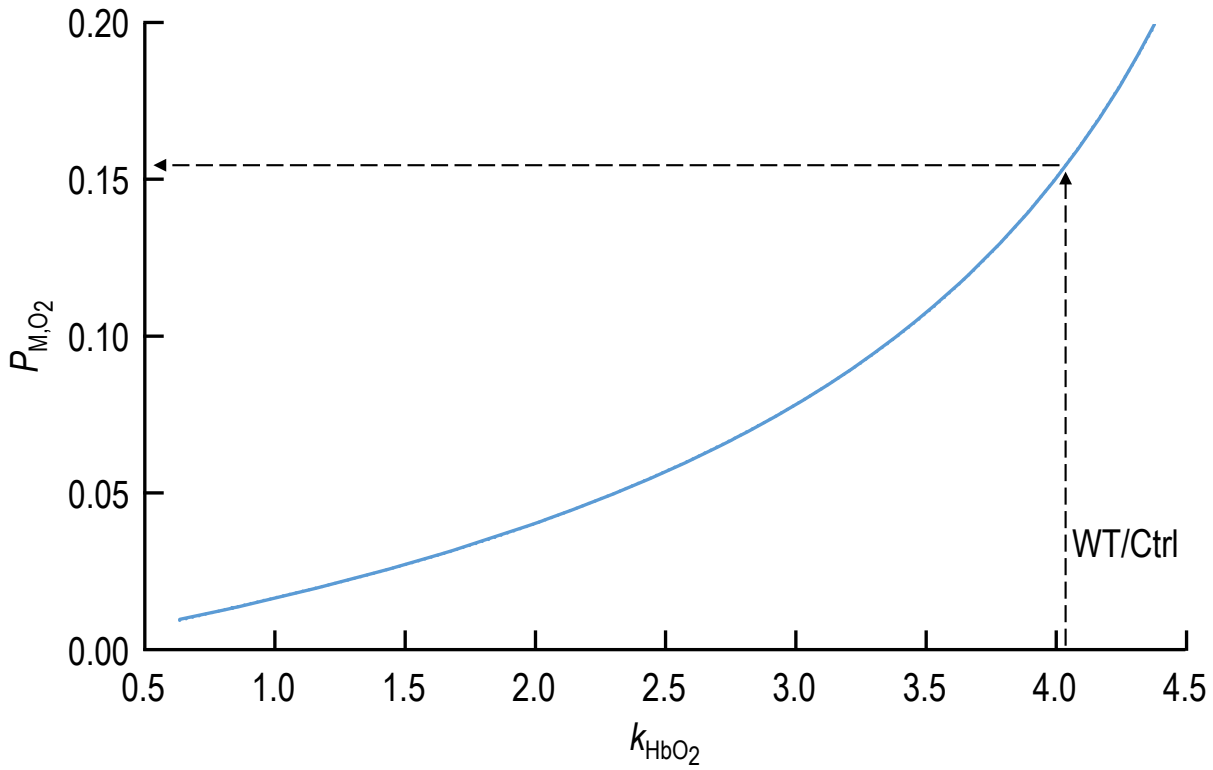

Figure 14. Inverted sigmoid plot

This figure is analogous to Figure 5 except that here we plot P_{M,O_2} on the y-axis, which is now linear, and the rate constant for deoxygenation of HbO_2, k_{HbO_2}, on the x-axis. The upward-sloping curve is a best fit created from a 5th-order polynomial. This is a convenient tool for interpolating P_{M,O_2} values that correspond to a particular k_{HbO_2} value as part of the rebalancing of P_{M,O_2}. The upward arrow illustrates how, for a wild-type BCD under control conditions (no drugs), we identify the point on the curve that corresponds to the P_{M,O_2} indicated by the leftward-pointing arrow.

References

Adair GS, Bock AV & Field H (1925). The hemoglobin system VI. the oxygen dissociation curve of hemoglobin. *J Biol Chem* **63,** 529–545.

Al-Samir S, Kyriazi D, Yool AJ, Moser I, Kyriazi K, Gros G, Tsiavaliaris G & Endeward V (2025). Aquaporin-1 acts as an O_2 channel. The permeability of human and mouse red cell membranes for oxygen. *Am J Physiol Cell Physiol*; DOI: 10.1152/ajpcell.00858.2024.

Blank M & Roughton FJW (1960). The permeability of monolayers to carbon dioxide. *Trans Faraday Soc* **56,** 1832–1841.

Boron WF (2010). Sharpey-Schafer lecture: Gas channels. *Exp Physiol* **95,** 1107–1130.

Boron WF, Endeward V, Gros G, Musa-Aziz R & Pohl P (2011). Intrinsic CO_2 permeability of cell membranes and potential biological relevance of CO_2 channels. *ChemPhysChem* **12,** 1017–1019.

Clark A, Federspiel WJ, Clark PA & Cokelet GR (1985). Oxygen delivery from red cells. *Biophys J* **47,** 171–181.

Coin JT & Olson JS (1979). The rate of oxygen uptake by human red blood cells. *J Biol Chem* **254,** 1178–1190.

Cooper GJ & Boron WF (1998). Effect of pCMBS on CO_2 permeability of *Xenopus* oocytes expressing aquaporin 1 or its C189S mutant. *Am J Physiol* **275,** C1481-1486.

Cooper GJ, Occhipinti R & Boron WF (2015). CrossTalk proposal: Physiological CO_2 exchange can depend on membrane channels. *J Physiol*; DOI: 10.1113/JP270059.

Deonikar P, Abu-Soud HM & Kavdia M (2014). Computational analysis of nitric oxide biotransport to red blood cell in the presence of free hemoglobin and NO donor. *Microvasc Res* **95,** 15–25.

Deonikar P & Kavdia M (2013). Contribution of membrane permeability and unstirred layer diffusion to nitric oxide-red blood cell interaction. *J Theor Biol* **317,** 321–330.

Endeward V (2012). The rate of the deoxygenation reaction limits myoglobin- and hemoglobin-facilitated O_2 diffusion in cells. *J Appl Physiol* **112,** 1466–1473.

Endeward V, Al-Samir S, Itel F & Gros G (2014). How does carbon dioxide permeate cell membranes? A discussion of concepts, results and methods. *Front Physiol* **4,** 382.

Endeward V, Musa-Aziz R, Cooper GJ, Chen L-M, Pelletier MF, Virkki LV, Supuran CT, King LS, Boron WF & Gros G (2006). Evidence that aquaporin 1 is a major pathway for CO_2 transport across the human erythrocyte membrane. *FASEB J* **20,** 1974–1981.

Fick A (1855). V. On liquid diffusion. *Lond Edinb Dubl Phil Mag* **10,** 30–39.

Forster RE (1964). Rate of gas uptake by red cells. In *Handbook of Physiology*, pp. 827–837. American Physiological Society.

Forstner H & Gnaiger E (1983). Appendix A. Calculation of equilibrium oxygen concentration. In *Polarographic oxygen sensors: aquatic and physiological applications*. Springer-Verlag, Berlin Heidelberg New York.

Geers C & Gros G (2000). Carbon dioxide transport and carbonic anhydrase in blood and muscle. *Physiol Rev* **80,** 681–715.

Gibson QH, Kreuzer F, Meda E & Roughton FJ (1955). The kinetics of human haemoglobin in solution and in the red cell at 37 degrees C. *J Physiol (Lond)* **129,** 65–89.

Graham T (1829). Notice of the singular inflation of a bladder. *Quart J Sci* **II,** 88–89.

Graham T (1833). XXVII. On the law of the diffusion of gases. *Lond Edinb Dubl Phil Mag* **2,** 175–190.

Han P & Bartels DM (1996). Temperature Dependence of Oxygen Diffusion in H_2O and D_2O. *J Phys Chem* **100,** 5597–5602.

Hartridge H & Roughton FJ (1927). The rate of distribution of dissolved gases between the red blood corpuscle and its fluid environment: Part I. Preliminary experiments on the rate of uptake of oxygen and carbon monoxide by sheep's corpuscles. *J Physiol (Lond)* **62,** 232–242.

Hess WR (1930). *Die regulierung des Blutkreislaufes: gleichzeitig ein Beitrag zur Physiologie des vegetativen Nervensystemes*. Thieme.

Holland RA, Shibata H, Scheid P & Piiper J (1985). Kinetics of O_2 uptake and release by red cells in stopped-flow apparatus: effects of unstirred layer. *Respir Physiol* **59,** 71–91.

Huffman DE, Occhipinti R, Somersalo E, Calvetti D & Boron WF (2025). A graphical user interface for "Role of channels in the O_2 permeability of murine red blood cells III. Mathematical modeling." Available at: https://doi.org/10.5281/zenodo.14932553.

Hughes JMB & Bates DV (2003). Historical review: the carbon monoxide diffusing capacity (DLCO) and its membrane (DM) and red cell (Theta.Vc) components. *Respir Physiol Neurobiol* **138,** 115–142.

Huxley VH & Kutchai H (1981). The effect of the red cell membrane and a diffusion boundary layer on the rate of oxygen uptake by human erythrocytes. *J Physiol (Lond)* **316,** 75–83.

Ivanov II, Fedorov GE, Gus'kova RA, Ivanov KI & Rubin AB (2004). Permeability of lipid membranes to dioxygen. *Biochem Biophys Res Commun* **322,** 746–750.

Kreuzer F (1982). Oxygen supply to tissues: the Krogh model and its assumptions. *Experientia* **38,** 1415–1426.

Krogh A (1919). The number and distribution of capillaries in muscles with calculations of the oxygen pressure head necessary for supplying the tissue. *J Physiol (Lond)* **52,** 409–415.

Kutchai H (1975). Role of the red cell membrane in oxygen uptake. *Respir Physiol* **23,** 121–132.

Lawson WH, Holland RA & Forster RE (1965). Effect of temperature on deoxygenation rate of human red cells. *J Appl Physiol* **20,** 912–918.

Michenkova M, Taki S, Blosser MC, Hwang HJ, Kowatz T, Moss FJ, Occhipinti R, Qin X, Sen S, Shinn E, Wang D-K, Zeise B, Zhao P, Malmstadt N, Vahedi-Faridi A, Tajkhorshid E & Boron WF (2021). Carbon dioxide transport across membranes. *Interface Focus* **11,** 2.

Mitchell JK (1830). On the penetrativeness of fluids. *Am J Med Sci* **7,** 36–67.

Mitchell JK (1833). Art. IX. On the penetration of gases. *Am J Med Sci* **13,** 100–112.

Moll W (1968). The influence of hemoglobin diffusion on oxygen uptake and release by red cells. *Respir Physiol* **6,** 1–15.

Moss FJ, Zhao P, Salameh AI, Taki S, Wass AB, Jacobberger JW, Huffman DE, Meyerson HJ, Occhipinti R & Boron WF (2025). Role of channels in the O_2 permeability of murine red blood cells II. Morphological and proteomic studies. *bioRxiv*; DOI: https://doi.org/10.1101/2025.03.05.639962.

Nakhoul NL, Davis BA, Romero MF & Boron WF (1998). Effect of expressing the water channel aquaporin-1 on the CO_2 permeability of *Xenopus* oocytes. *Am J Physiol* **274,** C543-548.

Nicolson P & Roughton FJW (1951). A theoretical study of the influence of diffusion and chemical reaction velocity on the rate of exchange of carbon monoxide and oxygen between the red blood corpuscle and the surrounding fluid. *Proc R Soc Lond, B, Biol Sci* **138,** 241–264.

Overton E (1895). Über die osmotischen Eigenschaften der Zelle in ihrer Bedeutung für die Toxikologie und Pharmacologie. *Z Phys Chem* **22,** 189–209.

Overton E (1899). Ueber die allgemeinen osmotischen Eigenschaften der Zelle, ihre vermutlichen Ursachen und ihre Bedeutung für die Physiologie. *Vierteljahrsschr Naturforsch Ges Zürich* **44,** 88–135.

Ponder E (1948). *Hemolysis and Related Phenomena*. New York : Grune & Stratton. Available at: http://hdl.handle.net/2027/wu.89047892849.

Popel AS (1989). Theory of oxygen transport to tissue. *Crit Rev Biomed Eng* **17,** 257–321.

Richardson SL, Hulikova A, Proven M, Hipkiss R, Akanni M, Roy NBA & Swietach P (2020). Single-cell O_2 exchange imaging shows that cytoplasmic diffusion is a dominant barrier to efficient gas transport in red blood cells. *PNAS* **117,** 10067–10078.

Roughton FJ, Adair GS, Barcroft J, Goldschmidt G, Herkel W, Hill RM, Keys AB & Ray GB (1936). The thermochemistry of the oxygen-haemoglobin reaction: Comparison of the heat as measured directly on purified haemoglobin with that calculated indirectly by the Van't Hoff Isochore. *Biochem J* **30,** 2117–2133.

Roughton FJW (1932). Diffusion and chemical reaction velocity as joint factors in determining the rate of uptake of oxygen and carbon monoxide by the red blood corpuscle. *Proc R Soc Lond B* **111,** 1–36.

Roughton FJW (1964). Transport of oxygen and carbon dioxide. In *Handbook of Physiology*, pp. 767–825. American Physiological Society.

Somersalo E, Occhipinti R, Boron WF & Calvetti D (2012). A reaction-diffusion model of CO_2 influx into an oocyte. *J Theor Biol* **309,** 185–203.

Stannett V (1978). The transport of gases in synthetic polymeric membranes—an historic perspective. *J Membrane Sci* **3,** 97–115.

Strutwolf J, Zhang J, Barker AL & Unwin PR (2001). Effect of phospholipids on the kinetics of dioxygen transfer across a 1,2-dichloroethane/water interface. *Phys Chem Chem Phys* **3,** 5553–5558.

Vandegriff KD & Olson JS (1984*a*). A quantitative description in three dimensions of oxygen uptake by human red blood cells. *Biophys J* **45,** 825–835.

Vandegriff KD & Olson JS (1984*b*). The kinetics of O_2 release by human red blood cells in the presence of external sodium dithionite. *J Biol Chem* **259,** 12609–12618.

Waisbren SJ, Geibel JP, Modlin IM & Boron WF (1994). Unusual permeability properties of gastric gland cells. *Nature* **368,** 332–335.

Williams JB & Kutchai H (1986). Use of a membrane-bound fluorophore to characterize diffusion boundary layers around human erythrocytes. *Biophys J* **49,** 453–458.

Wroblewski S (1879). On the nature of the absorption of gases. *Nature* **21,** 190–192.

Yamaguchi K, Nguyen-Phu D, Scheid P & Piiper J (1985). Kinetics of O2 uptake and release by human erythrocytes studied by a stopped-flow technique. *J Appl Physiol (1985)* **58,** 1215–1224.

Yap EW & Hellums JD (1987). Use of Adair Four-Step Kinetics in Mathematical Simulation of Oxygen Transport in the Microcirculation. In *Oxygen Transport to Tissue IX*, Advances in Experimental Medicine and Biology, pp. 193–207. Springer, Boston, MA. Available at: https://link.springer.com/chapter/10.1007/978-1-4684-7433-6_22 [Accessed May 18, 2018].

Zhao P, Moss FJ, Occhipinti R, Geyer RR, Huffman DE, Meyerson HJ & Boron W F (2025). Role of channels in the O_2 permeability of murine red blood cells. I. Stopped-flow and hematological studies. *bioRxiv*; DOI: 10.1101/2025.03.05.639948.

Additional Information

Data availability statement

The data that support the findings of this study are available from the corresponding authors, R.O. and W.F.B., upon reasonable request.

Competing interests

The authors declare that they have no competing interests.

Author contributions

R.O., P.Z. & W.F.B. designed the study; R.O. developed and implemented the computational model, and performed all numerical simulations; R.O., P.Z. and W.F. B. analyzed data. R.O., P.Z. & W.F.B. prepared the figures; R.O., P.Z., F.J.M., & W.F.B. wrote the manuscript.

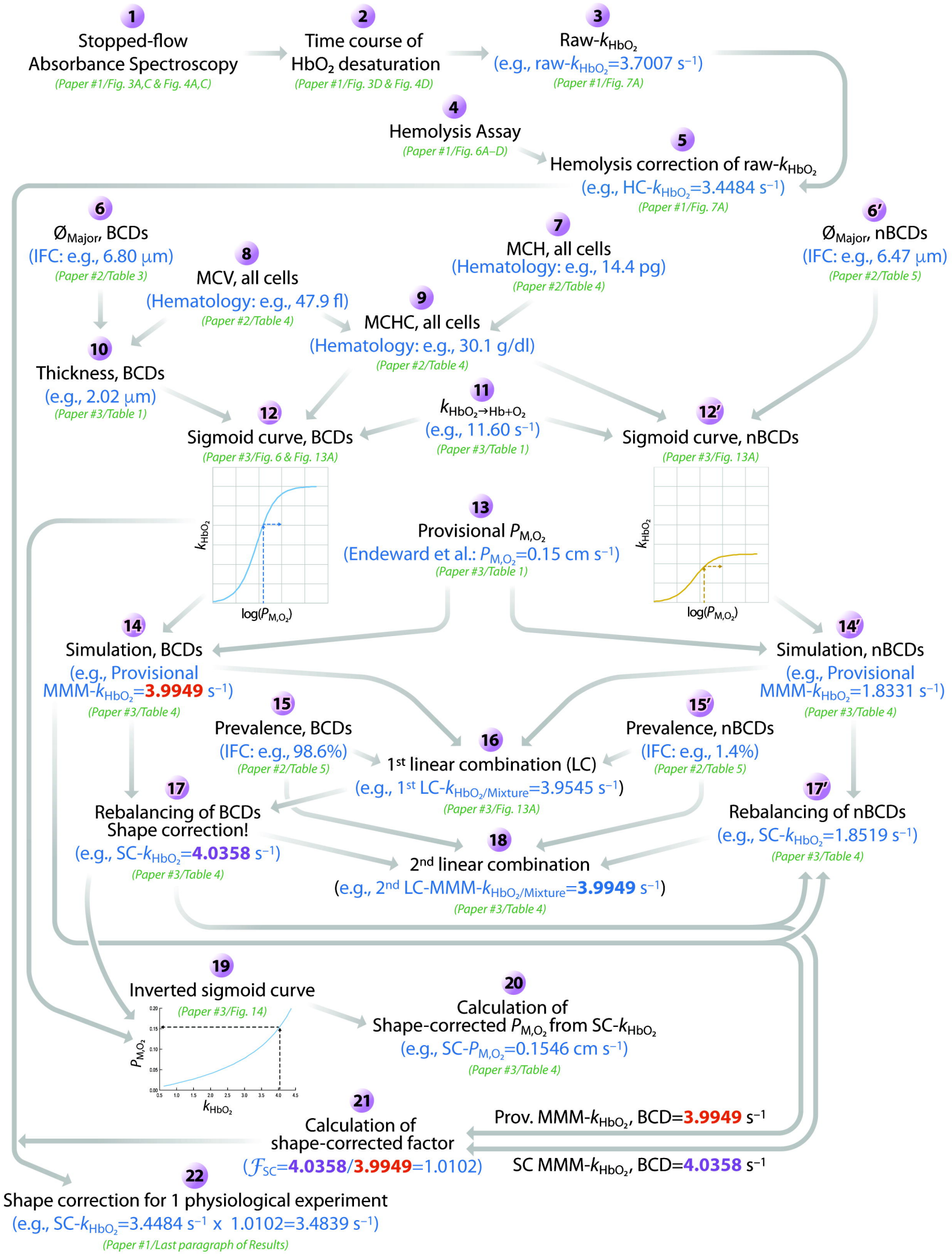
1
Stopped-flow Absorbance Spectroscopy
(Paper #1/Fig. 3A,C & Fig. 4A,C)
2
Time course of HbO_2 desaturation
(Paper #1/Fig. 3D & Fig. 4D)
3
Raw-k_{HbO_2}
(e.g., raw-k_{HbO_2}=3.7007 s^{-1})
(Paper #1/Fig. 7A)
4
Hemolysis Assay
(Paper #1/Fig. 6A–D)
5
Hemolysis correction of raw-k_{HbO_2}
(e.g., HC-k_{HbO_2}=3.4484 s^{-1})
(Paper #1/Fig. 7A)
6
$Ø_{Major}$, BCDs
(IFC: e.g., 6.80 μm)
(Paper #2/Table 3)
6′
$Ø_{Major}$, nBCDs
(IFC: e.g., 6.47 μm)
(Paper #2/Table 5)
7
MCH, all cells
(Hematology: e.g., 14.4 pg)
(Paper #2/Table 4)
8
MCV, all cells
(Hematology: e.g., 47.9 fl)
(Paper #2/Table 4)
9
MCHC, all cells
(Hematology: e.g., 30.1 g/dl)
(Paper #2/Table 4)
10
Thickness, BCDs
(e.g., 2.02 μm)
(Paper #3/Table 1)
11
$k_{HbO_2 \rightarrow Hb+O_2}$
(e.g., 11.60 s^{-1})
(Paper #3/Table 1)
12
Sigmoid curve, BCDs
(Paper #3/Fig. 6 & Fig. 13A)
12′
Sigmoid curve, nBCDs
(Paper #3/Fig. 13A)
k_{HbO_2}
$\log(P_{M,O_2})$
13
Provisional P_{M,O_2}
(Endeward et al.: P_{M,O_2}=0.15 cm s^{-1})
(Paper #3/Table 1)
14
Simulation, BCDs
(e.g., Provisional MMM-k_{HbO_2}=3.9949 s^{-1})
(Paper #3/Table 4)
14′
Simulation, nBCDs
(e.g., Provisional MMM-k_{HbO_2}=1.8331 s^{-1})
(Paper #3/Table 4)
15
Prevalence, BCDs
(IFC: e.g., 98.6%)
(Paper #2/Table 5)
15′
Prevalence, nBCDs
(IFC: e.g., 1.4%)
(Paper #2/Table 5)
16
1st linear combination (LC)
(e.g., 1st LC-$k_{HbO_2/Mixture}$=3.9545 s^{-1})
(Paper #3/Fig. 13A)
17
Rebalancing of BCDs
Shape correction!
(e.g., SC-k_{HbO_2}=4.0358 s^{-1})
(Paper #3/Table 4)
17′
Rebalancing of nBCDs
(e.g., SC-k_{HbO_2}=1.8519 s^{-1})
(Paper #3/Table 4)
18
2nd linear combination
(e.g., 2nd LC-MMM-$k_{HbO_2/Mixture}$=3.9949 s^{-1})
(Paper #3/Table 4)
19
Inverted sigmoid curve
(Paper #3/Fig. 14)
P_{M,O_2}
k_{HbO_2}
20
Calculation of Shape-corrected P_{M,O_2} from SC-k_{HbO_2}
(e.g., SC-P_{M,O_2}=0.1546 cm s^{-1})
(Paper #3/Table 4)
21
Calculation of shape-corrected factor
($\mathcal{F}_{SC}$=4.0358/3.9949=1.0102)
Prov. MMM-k_{HbO_2}, BCD=3.9949 s^{-1}
SC MMM-k_{HbO_2}, BCD=4.0358 s^{-1}
22
Shape correction for 1 physiological experiment
(e.g., SC-k_{HbO_2}=3.4484 s^{-1} x 1.0102=3.4839 s^{-1})
(Paper #1/Last paragraph of Results)

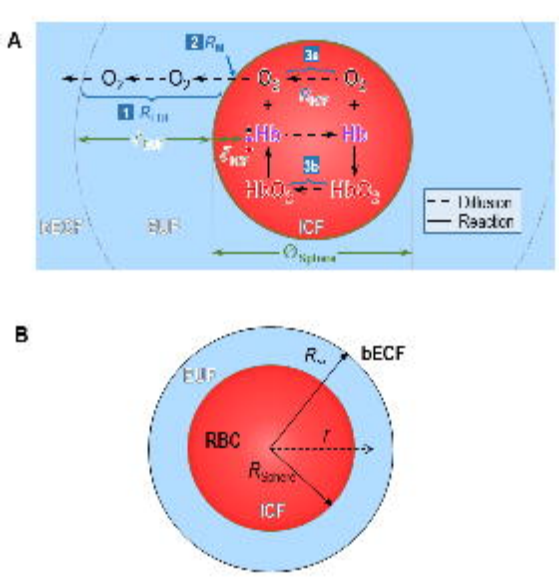
A
2 R_{M}
3a
O_2
O_2
O_2
O_2
1 R_{cap}
v_{cap}
v_{RBC}
HbO_2
Hb
v_{ICF}
3b
HbO_2
HbO_2
Diffusion
Reaction
bECF
SUP
ICF
O_{Sphere}
B
R_{∞}
bECF
SUP
RBC
r
R_{Sphere}
ICF

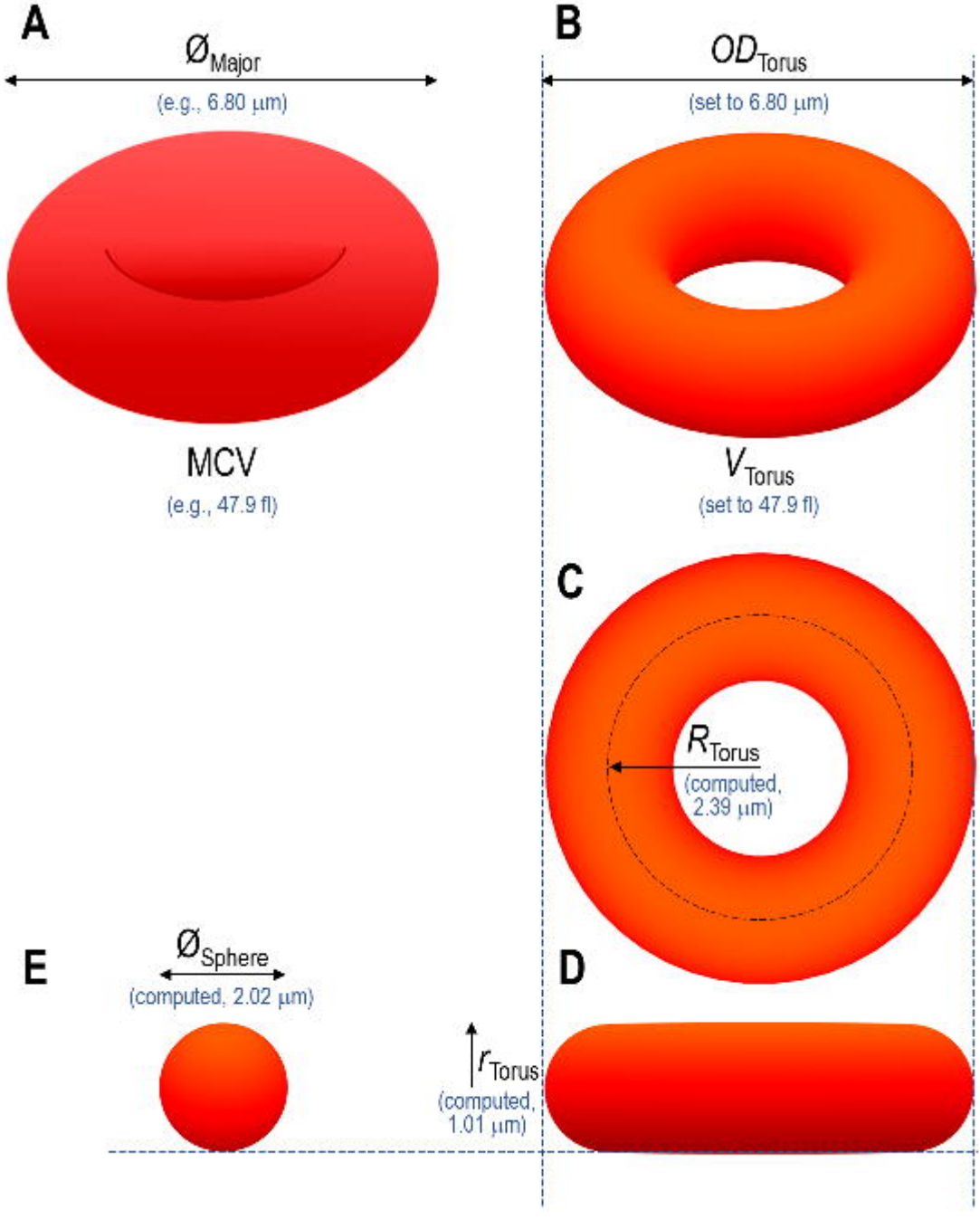
A
Ø Major
(e.g., 6.80 μm)
MCV
(e.g., 47.9 fl)
B
OD Torus
(set to 6.80 μm)
V Torus
(set to 47.9 fl)
C
R Torus
(computed, 2.39 μm)
D
r Torus
(computed, 1.01 μm)
E
Ø Sphere
(computed, 2.02 μm)

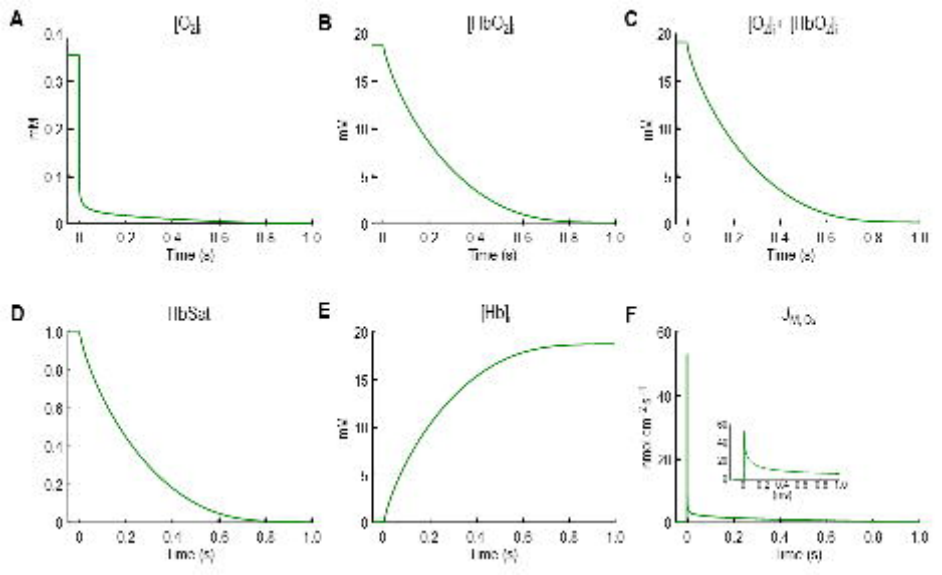
A
[O2]
mM
Time (s)
B
[HbO2]
mM
Time (s)
C
[O2] + [HbO2]
mM
Time (s)
D
HbSat
Time (s)
E
[Hb]
mM
Time (s)
F
Time (s)

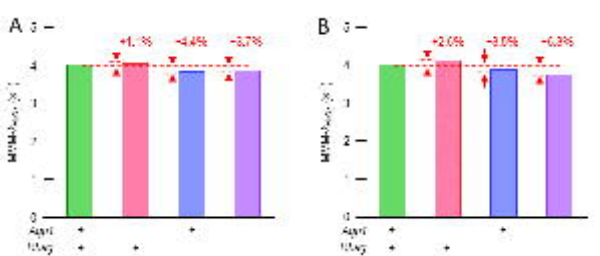
A
+1.1%
-4.4%
-3.7%
B
+2.0%
-3.0%
-0.3%

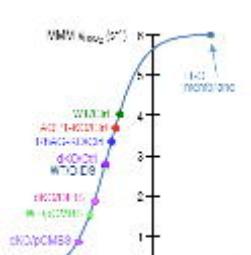
6
5
4
3
2
1
0.001
0.01
0.1
1
10
100

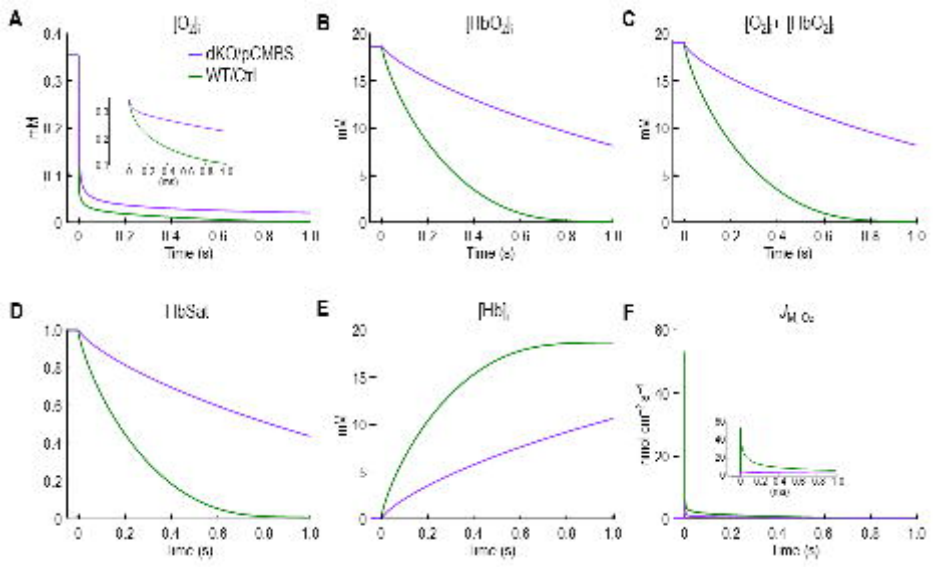
A
[O2]i
dKO/pCMBS
WT/Ctrl
mM
Time (s)
B
[HbO2]i
mM
Time (s)
C
[O2]i + [HbO2]i
mM
Time (s)
D
HbSat.
Time (s)
E
[Hb]i
mM
Time (s)
F
JM,O2
Time (s)

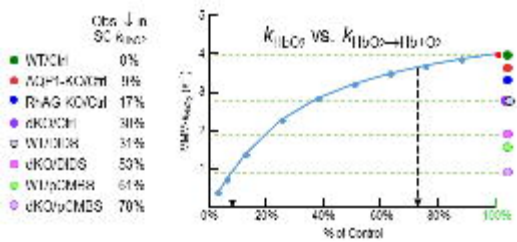

Obs ↓ in SC k_{HbO2}
WT/Ctrl 0%
AQP1-KO/Ctrl 9%
RhAG KO/Ctrl 17%
dKO/Ctrl 30%
WT/DIDS 31%
dKO/DIDS 53%
WT/pCMBS 61%
dKO/pCMBS 70%
k_{HbO2} vs. $k_{HbO2 \rightarrow Hb+O2}$
0%
20%
40%
60%
80%
100%
% of Control

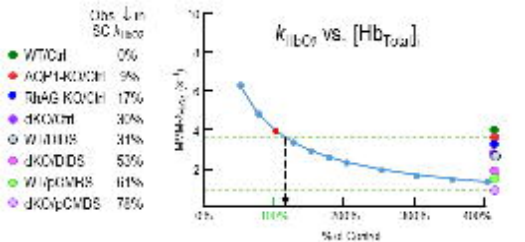

Obs. ↓ in SC k_{HbCO}
WT/Cut 0%
AQP1-KO/Ctrl 9%
RhAG KO/Ctrl 17%
dKO/Ctrl 30%
WT/DDS 31%
dKO/DDS 53%
WT/pCMRS 61%
dKO/pCMDS 78%
k_{HbCO} vs. $[Hb_{Total}]_i$
0%
100%
200%
300%
400%
% of Control

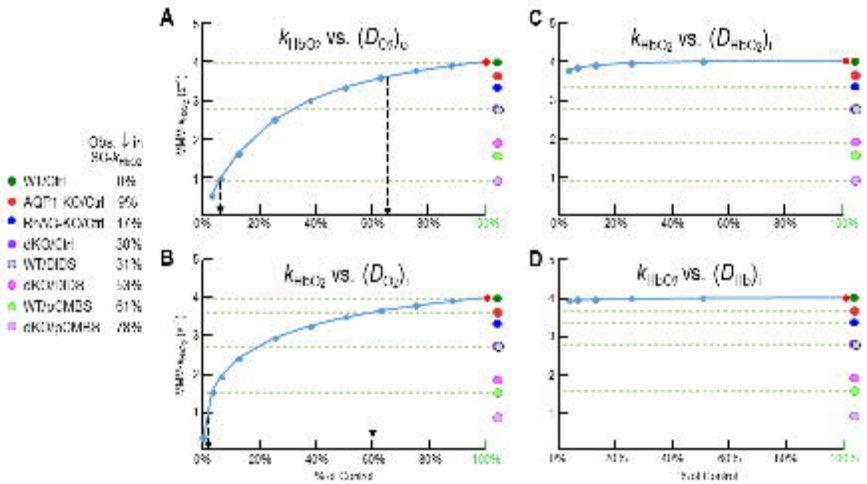

A
B
C
D
Obs. ↓ in SO-k_{HbO2}
WT/CtH 0%
AQP1 KO/CuI 9%
RhVC-KO/CtH 17%
dKO/CtH 30%
WT/DIDS 31%
dKO/DIDS 53%
WT/pCMBS 61%
dKO/pCMBS 78%
k_{HbO2} vs. $(D_{O2})_c$
k_{HbO2} vs. $(D_{HbO2})_i$
k_{HbO2} vs. $(D_{O2})_i$
k_{HbO2} vs. $(D_{Hb})_i$
0%
20%
40%
60%
80%
100%
% of Control

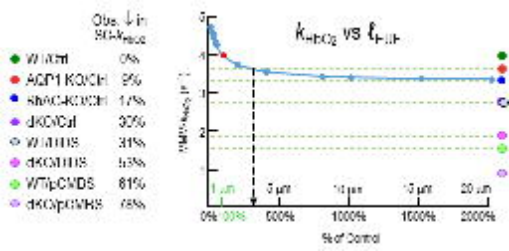

Obs. ↓ in SO-k_{HbO_2}
WT/Ctrl 0%
AQP1 KO/Ctrl 9%
RhAG-KO/Ctrl 17%
dKO/Ctrl 30%
WT/DDS 31%
dKO/DDS 53%
WT/pCMDS 61%
dKO/pCMBS 78%
k_{HbO_2} vs ℓ_{HbF}
1 μm
5 μm
10 μm
15 μm
20 μm
0%
100%
500%
1000%
1500%
2000%
% of Control

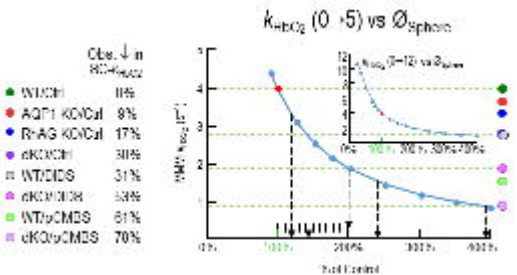

k_{HbO_2} (0 → 5) vs $Ø_{Sphere}$
Obs. ↓ in SO-k_{HbO_2}
WT/Ctrl 0%
AQP1 KO/Ctrl 9%
RhAG KO/Ctrl 17%
dKO/Ctrl 30%
WT/DIDS 31%
dKO/DIDS 53%
WT/pCMBS 61%
dKO/pCMBS 70%
Total Control

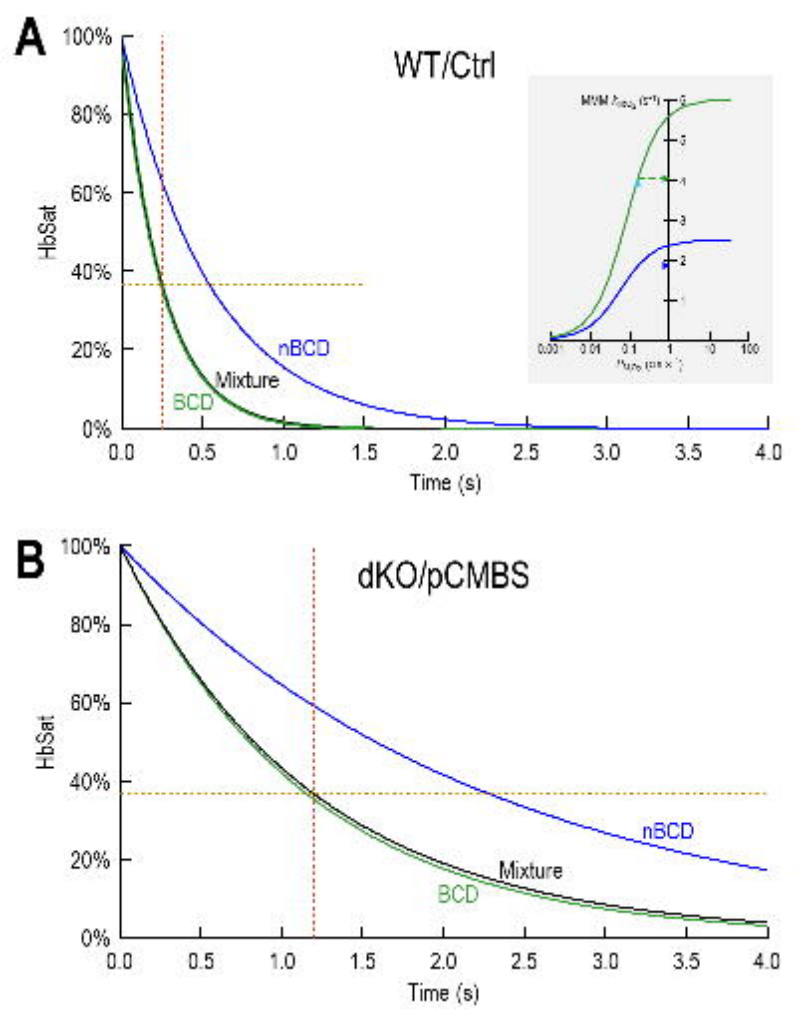
A
WT/Ctrl
HbSat
100%
80%
60%
40%
20%
0%
nBCD
Mixture
BCD
0.0
0.5
1.0
1.5
2.0
2.5
3.0
3.5
4.0
Time (s)
B
dKO/pCMBS
HbSat
100%
80%
60%
40%
20%
0%
nBCD
Mixture
BCD
0.0
0.5
1.0
1.5
2.0
2.5
3.0
3.5
4.0
Time (s)

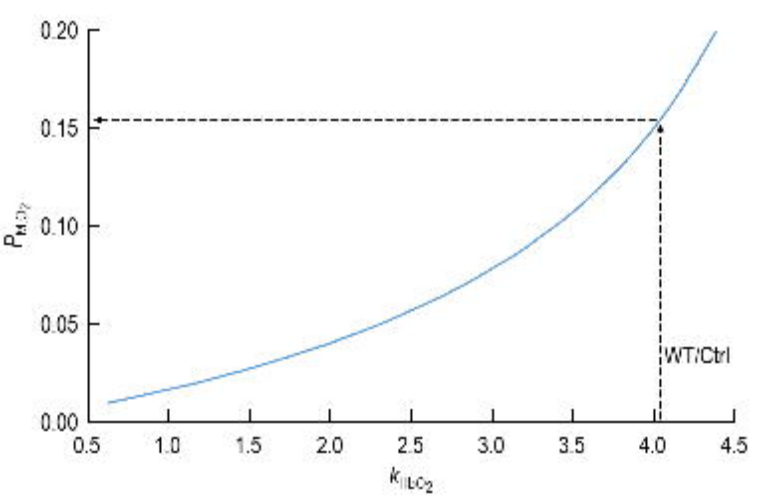
0.20
0.15
0.10
0.05
0.00
$P_{HCO_3^-}$
0.5
1.0
1.5
2.0
2.5
3.0
3.5
4.0
4.5
$k_{HCO_3^-}$
WT/Ctrl